

AD-A215 079

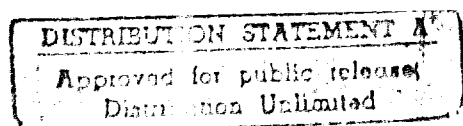
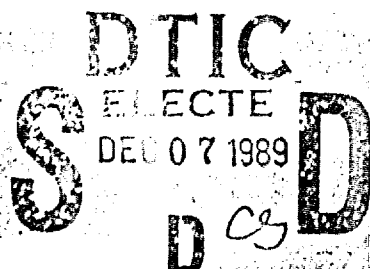
DEVELOPMENT OF A  
RECEIVER FOR A SPACE-  
BASED LASER RADAR  
SYSTEM

Final Technical Report for the Period  
September 1, 1988 to September 30, 1989

Contract No. N00014-88-C-0600  
Office of Naval Research  
800 North Quincy Street  
Arlington, VA 22217

J. Chantry, D. Bhasavanich, and I. Liberman  
Optical Physics & Directed Energy Research

October 15, 1989



BEST  
AVAILABLE COPY



Westinghouse STC  
1310 Beulah Road  
Pittsburgh, Pennsylvania 15235

89 11 21 145

# DEVELOPMENT OF A RECEIVER FOR A SPACE- BASED LASER RADAR SYSTEM

Final Technical Report for the Period  
September 1, 1988 to September 30, 1989

Contract No. N00014-88-C-0800  
Office of Naval Research  
800 North Quincy Street  
Arlington, VA 22217

P. J. Chantry, D. Bhasavanich, and I. Liberman  
Optical Physics & Directed Energy Research

October 15, 1989

Accession For	
NTIS CRA&I	<input checked="" type="checkbox"/>
DTIC TAB	<input type="checkbox"/>
Unannounced	<input type="checkbox"/>
Justification	
By <i>pr CS</i>	
Distribution/	
Availability Codes	
Dist	Avail and/or Special
<i>A-1</i>	



Westinghouse STC  
1310 Beulah Road  
Pittsburgh, Pennsylvania 15235

# CONTENTS

LIST OF FIGURES.....	v
1. INTRODUCTION AND SUMMARY.....	1
2. SYSTEM DESCRIPTION AND MODEL PREDICTIONS.....	3
3. EXPERIMENT.....	10
3.1 Apparatus.....	10
3.1.1 Cell Construction, Processing, and Filling.....	10
3.1.2 Experimental Arrangement.....	13
3.1.3 Fluorescence Detection System.....	15
3.2 Measurements of Relative Red Fluorescence Signals and Cs* and Tl <sub>2</sub> Lifetimes.....	18
3.3 Reconciliation of Measurements and Model Predictions Giving [Cs].....	20
3.4 Measurement of UV Fluorescence Giving [Tlm].....	27
3.5 Attempted Measurement of Cs* Transient Density.....	30
3.6 Derived Lower Limit for Energy Transfer Cross Section, $\sigma_2$ .....	33
4. RADIATION TRAPPING IN ENVELOPES WITH REFLECTING BOUNDARIES.....	35
5. CONCLUSIONS AND RECOMMENDATIONS.....	40
6. REFERENCES.....	41
7. ACKNOWLEDGMENTS.....	42
8. APPENDIX A.....	43

## LIST OF FIGURES

Figure 1.	Energy levels of Tl and Cs relevant to the filter operation.....	4
Figure 2.	General reaction scheme treated in the model of the Tl-Cs atomic line filter. P represents the optical pumping rate. Levels 1 and 2 are the resonance levels of Cs.....	6
Figure 3.	Photograph of the pyrex cell after being used in the present experiments, shown beside an unused empty cell.....	12
Figure 4.	Experimental arrangement used for pulse pumping of the Cs-Tl cell, measuring the resulting red fluorescence, and measuring the response of the pumped cell to a pulse of green light tuned to the 535 nm absorption line.....	14
Figure 5.	Oscilloscope traces of the red pump pulse, the green signal pulse, and the resulting red and UV fluorescence signals. The time scale of the red fluorescence trace is 200 ns/div., and for the other three traces is 10 ns/div.....	16
Figure 6.	Curve fitting to Cs fluorescence data.....	19
Figure 7.	UV fluorescence intensity vs. delay time, measured for two different temperature conditions of the cell. The temperature indicated on each graph is that of the cold spot.....	21
Figure 8.	Comparison of measured and predicted fluorescence lifetimes using baseline model parameters from Table 1. The points are from experiments at cold spot temperatures of 400°C (squares) and 430°C (circles).....	24
Figure 9.	Comparison of measured and fluorescence lifetimes and model predictions using adjusted quenching rates.....	26
Figure 10.	Reconciliation of measured UV intensity vs. 535 nm signal with theoretically predicted curve.....	29

- Figure 11. Predicted time dependence of the UV fluorescence signal, taking into account the trapping of the 378 nm line at the density of  $[Tl]=3.6 \times 10^{11} \text{ cm}^{-3}$  expected at the operating cold spot temperature of  $430^\circ\text{C}$ . The net radiative lifetime of the upper state under these conditions is 11.6 ns. The indicated pulse width  $W_p$  is the ratio of area to amplitude..... 31
- Figure 12. Data from Ingold (1968) replotted to illustrate the (1-R) dependence. T is the increase in imprisoned lifetime due to wall reflectivity R.  $T_0$  is the imprisoned lifetime for R=0. The parameter  $k_0 d$  is the optical depth at line center between the planar boundaries separated by d..... 36
- Figure 13. Data from Ingold (1968) replotted to illustrate empirically derived functional form of the dependence on  $k_0 d$ ..... 38
- Figure 14. Data from Ingold (1970) replotted using the functional form of the dependence on  $k_0 d$  derived empirically from Ingold's 1968 data, as illustrated in Figure 13..... 39
- Figure A1. Three-level system involved in the absorption of 535 nm photons by  $Tl_m$ , and the subsequent emission of 535 nm and 378 nm photons by the upper state. The A's represent transition probabilities, and  $\sigma$ 's are the stimulated absorption and emission cross sections. P is the optical power within the absorption linewidth in units of photons/cm<sup>2</sup>/s..... 44
- Figure A2. Predicted time dependences of the metastable and excited state densities normalized to the initial metastable density. The ordinate represents time measured in units of the net radiative lifetime of the upper state. The green pump pulse is assumed to last 4 ns..... 47

# 1. INTRODUCTION

This report summarizes work performed at the Westinghouse Science and Technology Center (formerly the Westinghouse R&D Center) under ONR Contract No. N00014-88-C-0600 for the period between September 1, 1988 and September 30, 1989. The objective of the contract was to perform basic measurements of quantities relevant to determining the engineering viability of a Tl-Cs atomic line filter (ALF) for use as a receiver in laser radar applications, and to enhance in other ways our ability to predict the performance of such cells, by improving the theoretical model.

A space-based laser radar system must be capable of operating in the presence of intense broadband background from the sun and other bright sources likely to be present in the field of view. Background immunity can be greatly enhanced by exploiting the narrow band feature of the laser transmitter, provided a matched narrow band receiver is available. An additional requirement is that the receiver have a sufficiently fast response for the system bandwidth not to be compromised.

These requirements are similar in many respects to those applicable to satellite-based laser communication systems, and previous work on the system of present interest was performed with a view toward using it for communicating through sea water from a satellite to a submarine at operational depths. Previous modeling has shown that the most significant unknown parameter in the operation of the cell is the cross section for transferring energy from  $\text{Cs}^*(6P)$  resonance states to Tl to create the thallium metastables,  $\text{Tl}_m$ , which form the basis of the cell's operation. Most of the present experimental work, described in Section 3, was directed toward measuring this cross section. It has provided a lower limit to the cross-section magnitude of  $6 \times 10^{-17} \text{ cm}^2$ , which is a factor of three larger than the value estimated from literature values for similar reactions.

In addition, analytical work was performed to develop an algorithm for including the effects of reflecting boundaries on the lifetime of the excitation associated with trapped radiation. This work is summarized in Section 4. The relevance of this to the Tl-Cs ALF is that the radiation associated with the  $\text{Cs}^*(6P)$  resonance states is strongly trapped, and we anticipate that reflecting surfaces would be incorporated in an engineered version in order to further reduce the level of pump power required. In addition, reflecting surfaces are likely to be used in order to direct the UV fluorescence signal to the output window of the cell under circumstances involving a moderate degree of trapping of the UV photons.

## 2. SYSTEM DESCRIPTION AND MODEL PREDICTIONS

The transmitter employs a flashlamp or laser diode-pumped solid-state Nd:BEL laser tuned such that its frequency-doubled output matches the major hyperfine component of the 535 nm absorption line in thallium. As seen in Figure 1, this absorption occurs between the metastable thallium level ( $6^2P_{3/2}$ ), hereafter referred to as  $Tl_m$ , lying approximately 1 eV above the ground state, and the  $7^2S_{1/2}$  state. This upper state has a natural radiative lifetime of 8 ns, with 47% decaying to the ground state by emission of a photon at 378 nm. This wavelength shift allows a straightforward choice of bulk glass pre- and post-filters such that the combination rejects all wavelengths other than at the hyperfine lines of the 535 nm transition. The output at 378 nm is in an ideal region for detection by a photomultiplier (PMT). It is sufficiently short for standard photocathodes to have high quantum efficiency, up to 30%, but is not so short as to limit the choice of output window material. The combination of glass pre- and post-filters, the wavelength converter cell, and the PMT detector constitutes an "atomic line filter" (ALF), various forms of which have been proposed (Anderson et al., 1989; Gelbwachs, 1988). In the Tl-Cs system, a primary technical issue is whether it is possible to sustain the required density of  $Tl_m$  in a suitably dimensioned absorption cell; the present work is an extension of previous work addressing this issue. The present approach, represented in Figure 1, involves creating  $Tl_m$  by collisional transfer of energy from Cs atoms optically pumped to their 6P resonance states by radiation at 852 and/or 894 nm. These resonance lines can be trapped within the cell provided the Cs density is sufficiently high, thereby extending the effective lifetimes of the Cs(6P) states.

The design of a Tl-Cs cell for a particular application involves first choosing the cell aperture to meet the system needs, then



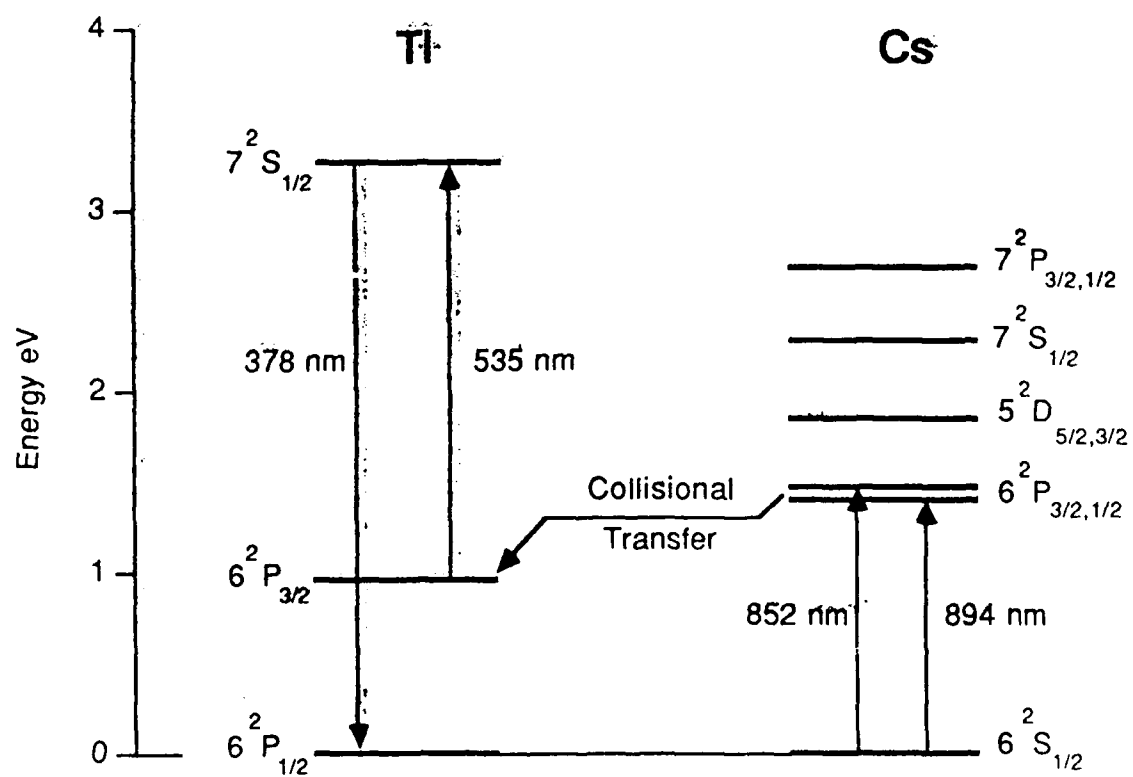


Figure 1. Energy levels of Tl and Cs relevant to the filter operation.

choosing the cell length to accommodate the provision of the required optical pump power through the curved sidewall, and then optimizing the atomic densities of Tl, Cs, and buffer gas to minimize the total pump power requirement. A computer model of the cell has been developed to help perform this optimization and has been described in detail previously (Chantry et al., 1988). The model treats the general reaction scheme represented in Figure 2. Level 1 is the Cs resonance level to which the pump light is tuned. The number of atoms pumped in this way, per unit volume, per unit time, is prescribed as P. Unless otherwise stated we assume level 1 to be the Cs( $6^2P_{3/2}$ ) level, pumped at 852 nm. Level 2 is then the nearby lower Cs( $6^2P_{1/2}$ ) state. Both these states can collisionally transfer their energy to Tl, forming Tl<sub>n</sub>. The various K's indicated in the figure represent the net frequencies for converting from one state to another, and in general are lumped quantities representing more than one process.

The processes relevant to the Tl-Cs filter operation are listed in Table 1 together with their respective cross sections. In general, the most important of these in determining the required pump power are (1) the absorption cross section of Tl<sub>n</sub> at 535 nm, which determines the required density of Tl<sub>n</sub>, and (2) the cross section for energy transfer from Cs(6P) to Tl, to form Tl<sub>n</sub>. The pump power requirement is found to have a first order dependence on these cross sections. Considerable uncertainty is attached to the value indicated in Table 1 for the energy transfer cross section, since it is an estimate based on the general trend of such cross sections with energy defect (Czajkowski et al., 1973). The primary objective in the present work was to reduce this uncertainty by making measurements in a Tl-Cs cell from which to derive this cross section. Also important but having a weaker effect are the cross sections for quenching of Tl<sub>n</sub> by Cs (reaction 5), and for energy exchange between the two Cs(6P) states (reaction 15). The latter has an effect because one of the resonance lines is more efficiently trapped than the other. A second objective in the present work was to measure the lifetimes of the Cs\*(6P) states, and of the Tl<sub>n</sub> under controlled conditions, and confirm the values predicted by the model.

The model has been applied to various sizes of right circular cylindrical cells, having diameters x lengths ranging from 20x40 cm, to

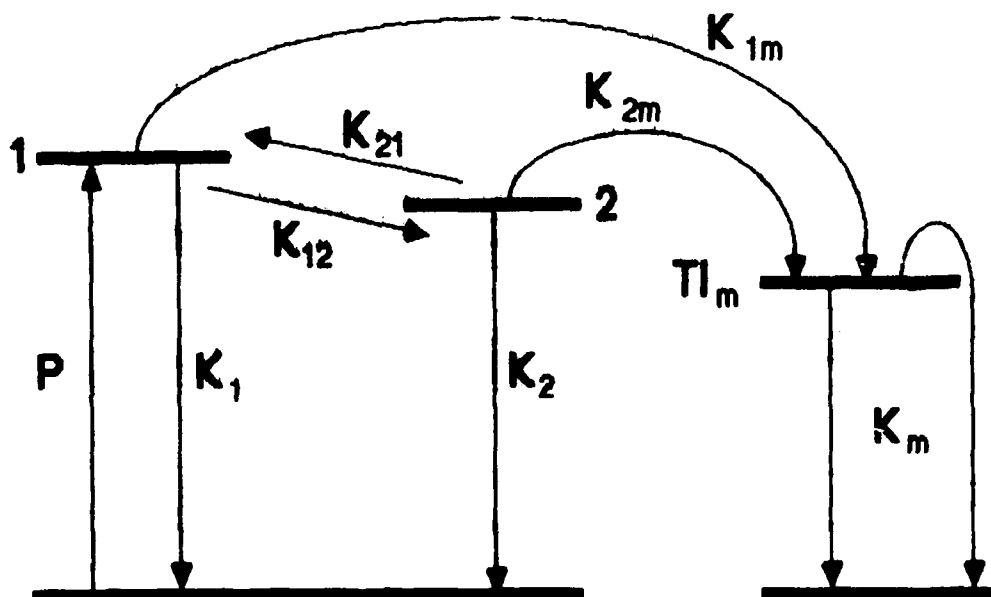


Figure 2. General reaction scheme treated in the model of the Tl-Cs atomic line filter.  $P$  represents the optical pumping rate. Levels 1 and 2 are the resonance levels of Cs.

Table 1  
Reactions Included in the Tl-Cs ALF Model

	Reaction	Cross Section (cm <sup>2</sup> )	Ref.
1	$\text{Cs}(6^2\text{S}_{1/2}) + h\nu (852 \text{ nm}) \rightarrow \text{Cs}^*(6^2\text{P}_{3/2})$ $+ h\nu (894 \text{ nm}) \rightarrow \text{Cs}^*(6^2\text{P}_{1/2})$	$\sigma_1(1) = 3.2 \times 10^{-11}$ $\sigma_1(2) = 1.7 \times 10^{-11}$	a a
2	$\text{Cs}^*(6^2\text{P}) + \text{Tl}(6^2\text{P}_{1/2}) \rightarrow \text{Tl}_m(6^2\text{P}_{3/2}) + \text{Cs}(6^2\text{S}_{1/2}) + \Delta E$	$\sigma_2 = 2 \times 10^{-17}$	b
3	$\text{Tl}_m(6^2\text{P}_{3/2}) + h\nu (535 \text{ nm}) \rightarrow \text{Tl}^*(7^2\text{S}_{1/2})$	$\sigma_3 = 5.2 \times 10^{-12}$	a
4	$\text{Tl}(6^2\text{P}_{1/2}) + h\nu (378 \text{ nm}) \rightarrow \text{Tl}^*(7^2\text{S}_{1/2})$	$\sigma_4 = 3.6 \times 10^{-12}$	a
5	$\text{Tl}_m(6^2\text{P}_{3/2}) + \text{Cs}(6^2\text{S}_{1/2}) \rightarrow \text{Tl}(6^2\text{P}_{1/2}) + \text{Cs}(6^2\text{S}_{1/2}) + \Delta E$	$\sigma_5 = 5 \times 10^{-18}$	b
6	$\text{Tl}_m(6^2\text{P}_{3/2}) + \text{Tl}(6^2\text{P}_{1/2}) \rightarrow 2\text{Tl}(6^2\text{P}_{1/2}) + \Delta E$	$\sigma_6 = 5 \times 10^{-16}$	c
7	$\text{Cs}^*(6^2\text{P}) + \text{Tl}(6^2\text{P}_{1/2}) \rightarrow \text{Tl}(6^2\text{P}_{1/2}) + \text{Cs}(6^2\text{S}_{1/2}) + \Delta E$	$\sigma_7 = 5 \times 10^{-18}$	b
8	$\text{Cs}^*(6^2\text{P}) + \text{Cs}(6^2\text{S}_{1/2}) \rightarrow 2 \text{Cs}(6^2\text{S}_{1/2}) + \Delta E$	$\sigma_8 = 8 \times 10^{-15}$	d
9	$\text{Cs}^*(6^2\text{P}) + \text{Cs}^*(6^2\text{P}) \rightarrow \text{Cs}^{**}(6\text{D}) + \text{Cs}(6\text{S}) + \Delta E$	$\sigma_9 = 1.5 \times 10^{-15}$ $- 2 \times 10^{-14}$	e
10	$\text{Cs}^*(6^2\text{P}) + h\nu (378 \text{ nm}) \rightarrow \text{Cs}^+ + e$	$\sigma_{10} = 1 \times 10^{-19}$	f
11	$\text{Cs}^*(6^2\text{P}) + \text{Tl}^*(7^2\text{S}_{1/2}) \rightarrow \text{Cs}^+ + \text{Tl}(6^2\text{P}_{1/2}) + e$	$\sigma_{11} = 5 \times 10^{-14}$	g
12	$\text{Cs}^*(6\text{P}) + \text{Cs}^*(6\text{P}) \rightarrow \text{Cs}_2^+ + e$	$\sigma_{12} = 1.1 \times 10^{-15}$	h
13	$\text{Tl}_m(6^2\text{P}_{3/2}) + \text{Kr} \rightarrow \text{Tl}(6^2\text{P}_{1/2}) + \text{Kr} + \Delta E$	$\sigma_{13} = 1.2 \times 10^{-22}$	j
14	$\text{Cs}^*(6^2\text{P}) + \text{Kr} \rightarrow \text{Cs}(6^2\text{S}_{1/2}) + \text{Kr} + \Delta E$	$\sigma_{14} = 1 \times 10^{-19}$	k
15	$\text{Cs}^*(6^2\text{P}_{3/2}) + \text{Cs}(6^2\text{S}_{1/2}) \rightarrow \text{Cs}^*(6^2\text{P}_{1/2}) + \text{Cs}(6^2\text{S}_{1/2}) + \Delta E$	$\sigma_{15} = 1.3 \times 10^{-14}$ $3.5 \times 10^{-15}$	d m
16	$\text{Cs}^*(6\text{P}_{3/2}) + \text{Kr} \rightarrow \text{Cs}^*(6\text{P}_{1/2}) + \text{Kr} + \Delta E$	$\sigma_{16} = 4 \times 10^{-22}$	n

(Footnotes to Table 1)

- a From transition A value, calculated for center of a Doppler broadened line at  $T=400^\circ\text{C}$ .
- b Estimated from energy defect, based on Fig 8 of Czajkowski et al. (1973).
- c Average of values from Pickett and Anderson (1969), and Aleksandrov et al. (1978), of  $5.4 \times 10^{-16}$  and  $4.5 \times 10^{-16} \text{ cm}^2$  respectively.
- d Derived from data previously reported. See Liu et al. (1986).
- e See Borodin and Komarov (1974).
- f Estimated from ionization cross section of Cs ground state. See Marr and Creek (1968).
- g Conservative (i.e. very high) estimate.
- h See Klyucharov and Ryzanov (1971). Essentially the same value is obtained by using the energy defect of  $\geq 0.07 \text{ eV}$  calculated from Korchevoy and Hiiko (1977) in method (b) above.
- j Aleksandrov et al. (1978)
- k Based on upper limit given by Dodd et al. (1969).
- m See Czajkowski and Krause (1965).
- n Scaled for  $T=400^\circ\text{C}$  from Fig. 2 of Gallagher (1968).

1x3 cm. Three examples are shown in Table 2. The largest cell is of interest for use in a submarine receiver where a large aperture and field of view is necessary, while the smallest cell would be more appropriate for applications where a small field of view would suffice, as in a laser radar application. In each case the design parameters shown in Table 2 have been selected to provide an adequate optical depth at 535 nm, while minimizing the pump power requirements.

In all cases the choice of Cs density involves a compromise between the desire to increase the effective lifetime of the  $\text{Cs}^*(6P)$  states, trapping of their associated resonance radiation, and the adverse effect of collisional quenching of  $\text{Tl}_\text{a}$  by Cs. Similarly, the choice of buffer gas (Kr) and its density involves a compromise between the increased effective lifetime of  $\text{Tl}_\text{a}$ , achieved by slowing their

Table 2  
Pumping and Temperature Requirements  
for Various Size Tl-Cs ALF Cells

Cell Size		Cell Temp. °K	Specie Densities				535 nm FWHM mÅ	Pump Power Required			
D cm.	L cm		[Tl] cm-3	[Cs] cm-3	[Kr] cm-3	[Tlm] cm-3		W/liter	W	mW/cm2 Sidewall	mW/cm2 Aperture
20	40	673	1.0E11	2.5E13	8.0E16	5.0E9	7	19	239	95	760
3	10	730	1.0E12	8.0E13	5.0E17	2.0E10	8	117	8.3	88	1170
1	3	775	5.0E12	2.0E14	1.0E18	6.0E10	11	469	1.1	120	1400

diffusive loss to the walls, and the reduction of the trapped lifetime of the Cs\*(6P) states caused by the collisional broadening of these transitions by the buffer gas. Increasing the Tl density has the desirable effect of increasing the rate of production of Tl<sub>2</sub> by collisional transfer from Cs\*(6P), thereby reducing the required density of the latter, and consequently also reducing the required pump power. Too high a Tl density causes the output photons at 378 nm to be trapped, forcing more of the upper state decay to occur via reemission of 535 nm photons, and again a compromise must be made. These considerations lead to the optimized densities indicated in Table 2 for the various sized cells.

We note that smaller cells require higher operating temperatures to achieve the higher Tl densities indicated. Thus it becomes important to establish the usable temperature range of the available envelope materials. High-temperature Cs compatibility tests performed prior to the present program identified Pyrex 7740 as a promising candidate, and we therefore chose to investigate this material further with a view toward using it for Tl-Cs cells.

### 3. EXPERIMENT

The primary objective of the experimental work was to determine the cross section for transfer of energy from the Cs\* resonance states to Tl to form the metastable. To do this required that we measure the density of Tl<sub>m</sub> produced in a known time by a known density of Cs\* when reacting with a known density of Tl. The difficulty in making this measurement lies in the fact that, *a priori*, only the Tl density can be predicted with any level of confidence from the operating parameters of the experiment. Thus we are faced with determining the absolute densities of both the reactant Cs\* and the product Tl<sub>m</sub>, and their time dependences. Furthermore, because the ground state Cs density is also unknown, due to the depression of its vapor pressure when alloyed with Tl, we cannot straightforwardly predict the effective lifetimes of the excited species from our theoretical model. Instead we must use the model interactively to reconcile the various measured quantities, and thereby derive the ground state Cs density.

#### 3.1 APPARATUS

##### 3.1.1 Cell Construction, Processing, and Filling

One of the objectives was to confirm the lifetimes of the active species predicted by the theoretical model, under operating conditions close to those anticipated in an operating filter. We therefore chose to use a cell of intermediate size relative to those considered in Section 2 (see Table 2), filled with the appropriate density of Kr buffer gas. The Tl-Cs alloy recipe, 1 wt% of Cs, is based on our previous mass spectrometric measurements (Chen et al., 1988). From our previous experience with metal cells, we were confident that we could operate this size of glass cell at temperatures in the vicinity of 400°C for extended periods of time and obtain useful densities of Cs and Tl. However, we are not able at present to confidently predict the exact density of Cs as a function of temperature, but the Tl density is expected to be close to that given by pure Tl.

A photograph of two glass cells is shown in Figure 3. They are essentially identical in size, having inside dimensions of  $D=8.6$  cm,  $L=27.3$  cm. They are made from a pyrex tube to which are sealed window quality end plates and two diametrically opposed side windows ( $D=5$  cm) situated at the middle of the tube. A short side tube protrudes from the bottom of the cell for containment of the condensed phase metal alloy. In operation, the temperature of this side tube is held at a temperature typically  $20^{\circ}\text{C}$  lower than the rest of the cell, thereby ensuring that it operates as the "cold spot" in determining the metal vapor densities. A second tube placed diametrically opposite the cold spot tube is used for pumping the cell during vacuum processing and provides access for loading the metal charges into the cell. The cell shown on the left in Figure 3 was used for the present experiment and is shown here in the condition prevailing after use. This involved continuous operation at a temperature above  $400^{\circ}\text{C}$  for 4500 hrs. Within that time the cell was held at  $\sim 450^{\circ}\text{C}$  for 3200 hrs. The retained optical quality of the envelope can be judged by comparison with the unused cell shown to the right of the photograph. We conclude that pyrex 7740 is a suitable envelope for a Tl-Cs ALF.

The sequence of events in processing and filling the cell was as follows:

- 1) The cell received from our glass shop was first flushed with reagent grade acetone and then with spectranalyzed methanol.
- 2) The cell was connected to a liquid nitrogen trapped diffusion pump station through an attached vacuum valve and baked under vacuum for a period of 22 hrs with the temperature held at over  $450^{\circ}\text{C}$  for more than 3 hrs.
- 3) After cooling, the cell was sealed with its attached valve, removed from the pumping station, and placed within the controlled Ar atmosphere glove box together with the vials of Tl and Cs to be used to load the cell.





Figure 3. Photograph of the Pyrex cell after being used in the present experiments, shown beside an unused empty cell.

- 4) The glove box gas drying and recirculation system was allowed to repurify the atmosphere until the indicated moisture level was in the satisfactory range ( $<10$  ppm), and the vacuum valve was opened allowing the cell to backfill with Ar. The vacuum valve was then temporarily removed to provide access. At this point a vial of Cs was opened and exposed to the glove box atmosphere. The exposed Cs retained its clean metallic appearance, indicating that the quality of the glove box atmosphere was sufficient for us to proceed with the cell filling.
- 5) The preweighed (10 g) purified Tl was removed from its ampoule and loaded into the cold spot sidearm. The Cs was injected through the sidearm using a calibrated syringe to provide the required measure (0.1 g).
- 6) The vacuum valve was reattached and closed. The cell was then removed from the glove box, reconnected to the vacuum pumping station, and reevacuated. The cell was then backfilled with 4 Torr of research-grade Kr, measured by a capacitance manometer, and tipped off leaving a short stub sidearm.

The sealed cell was then installed in an oven with thermocouples attached at the cold spot tube and two other positions on the main cell body. The cell was supported on shaped firebricks at the center of the oven, which has independently controllable heaters situated on the oven floor, the top wall, and around each of the four windows with which the cell is aligned during installation. The cell cold spot side tube was enclosed by fire brick material through which cooling nitrogen gas could be passed in order to reduce the cold spot temperature as desired.

### 3.1.2 Experimental Arrangement

The arrangement of the cell, its oven, and the various optical components used in the experiment, is represented in Figure 4. The cell is pumped at either 852 or 894 nm using a tunable dye laser (Quanta Ray Model DCR/PDL), pumped by a Nd-YAG laser which is flash-lamp pumped, Q switched, and frequency doubled to 532 nm for pumping the dye laser.

# TI-Cs ALF EXPERIMENTAL SETUP

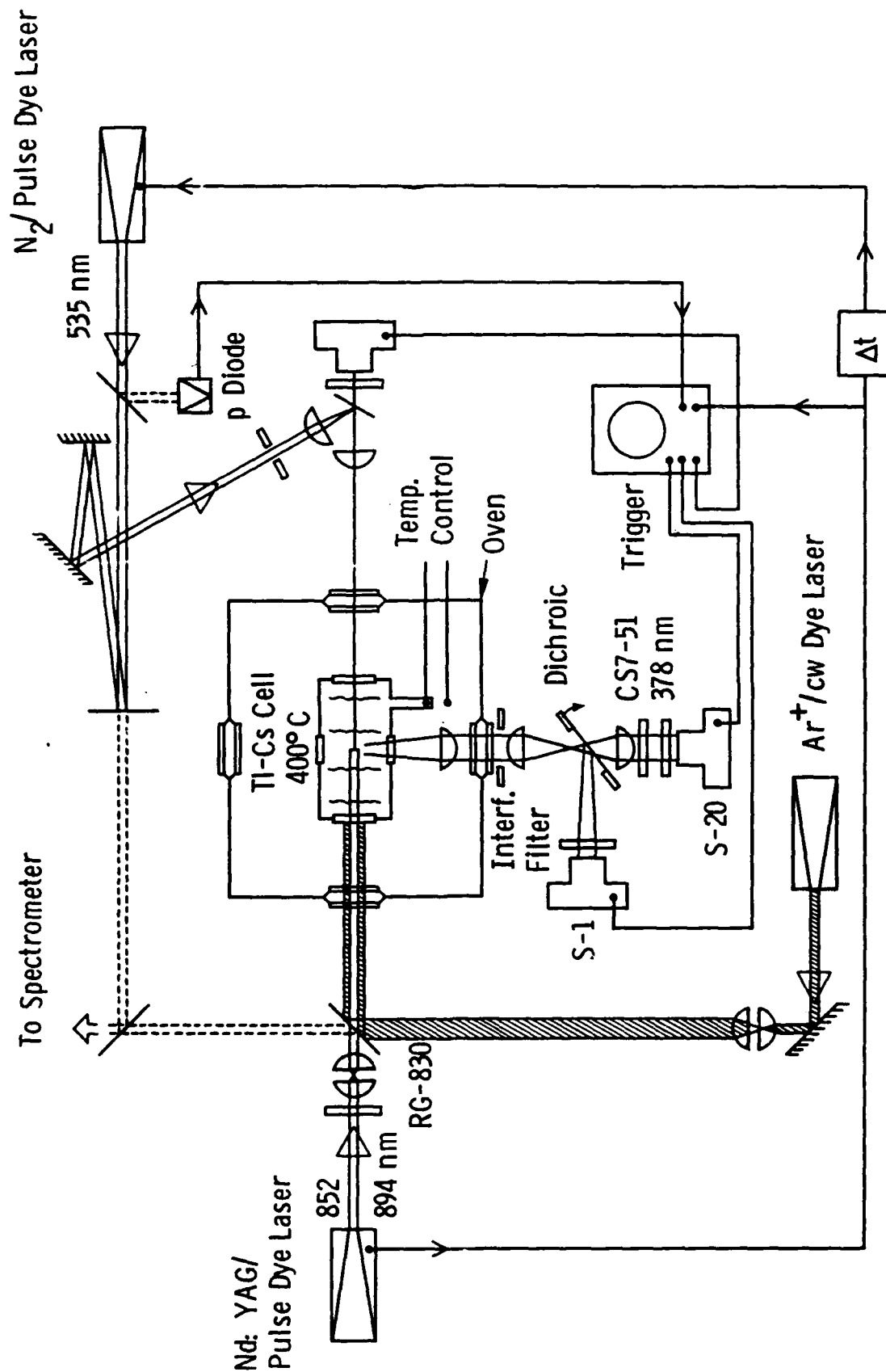


Figure 4. Experimental arrangement used for pulse pumping of the Cs-Tl cell, measuring the resulting red fluorescence, and measuring the response of the pumped cell to a pulse of green light tuned to the 535 nm absorption line.

The pulsing circuitry provides synchronizing pulses for external control of other components of the experiment. The 10 Hz pulses last  $<10$  ns, with a peak power of  $>10^5$  W/cm<sup>2</sup>. An example of an oscilloscope record, obtained from a Hamamatsu R1193U-01 vacuum diode having a response time of  $<1$  ns, is shown in Figure 5. An RG830 glass filter excludes wavelengths shorter than 800 nm from the laser output beam. The beam is steered and, if desired, expanded using two confocal lenses of appropriate focal lengths. The red beam is first carefully aligned with the cell axis, and coincidence of the pumped region and the region viewed by the PMTs is checked by successively blocking the upper and lower halves of the pump beam and requiring that the amplitude of the detected red fluorescence be the same in each case.

The 535 nm green pulses are supplied by a dye laser (Molelectron Model 200) pumped by a pulsed N<sub>2</sub> laser synchronized to the pump laser with a controlled delay. An oscilloscope record of this pulse, obtained with the same vacuum photodiode, is shown to the right in Figure 5. A small fraction of the green beam is split off and detected by a vacuum photodiode, the output of which was used to trigger the oscilloscope when viewing the UV fluorescence from the cell. A second beam splitter transports part of the beam to a spectrometer to facilitate initial tuning of the laser to the 535 nm absorption line. The main green beam is allowed to expand for a few meters before "cleaning" it with an 8 mm circular aperture. For most of the measurements two simple lenses were used to compress the beam to a diameter of  $<1$  mm before passing it into the oven and cell. Measurements of the beam size before and after the oven indicated that the beam retained its size over that distance.

Overlap of the red and green beams is carefully checked at both oven windows, ensuring that the beams also overlap within the cell. In any event, tests indicate that the production of the UV fluorescence is only weakly sensitive to the degree of beam overlap. This insensitivity was expected because of the relatively large red beam and the tendency for the resonance excitation of the Cs to diffuse away from the region initially excited.

### 3.1.3 Fluorescence Detection System

The central region of the cell is viewed by an optical system which images the axis of the cell at the center of a rotatable beam

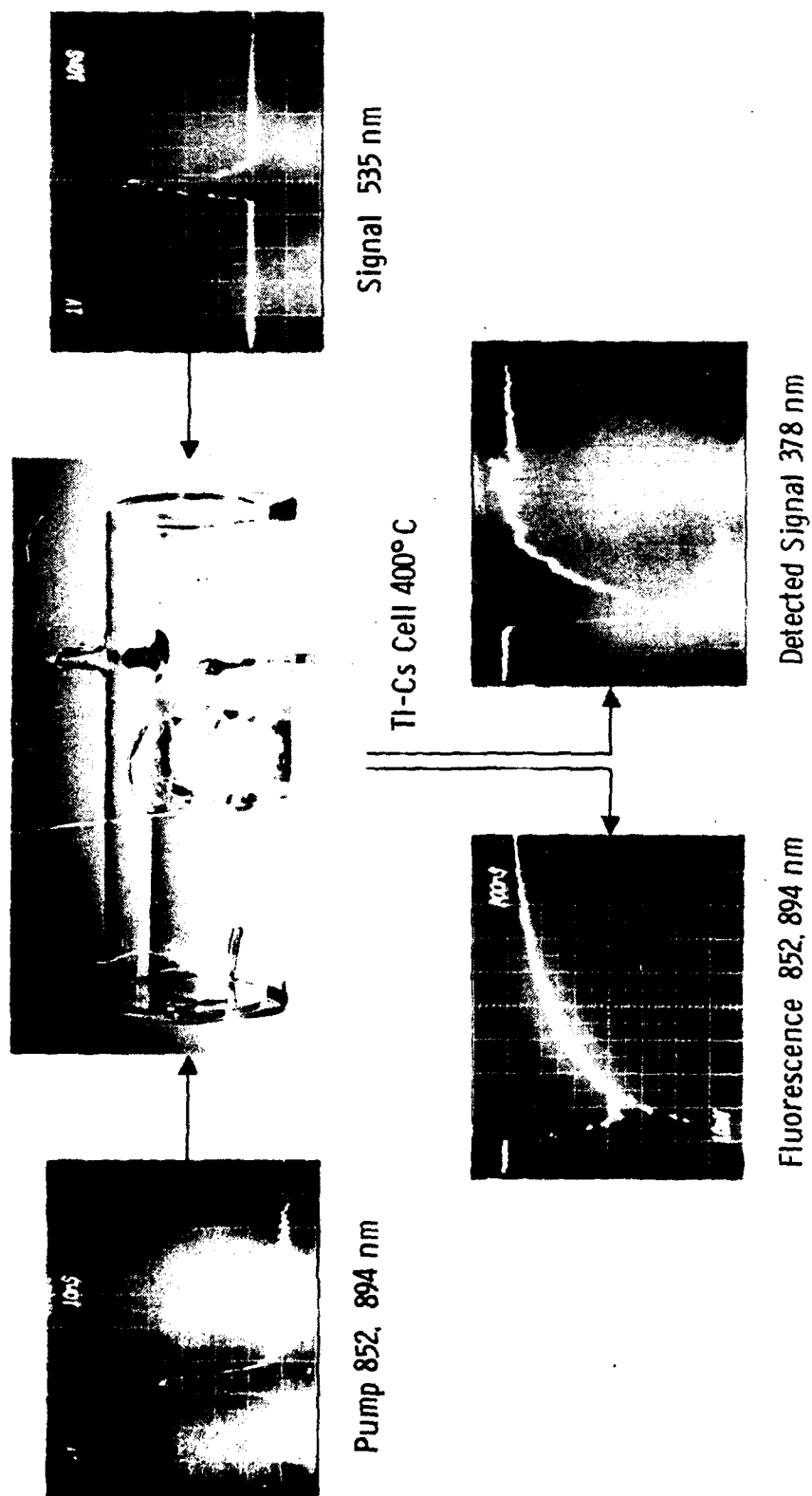


Figure 5. Oscilloscope traces of the red pump pulse, the green signal pulse, and the resulting red and UV fluorescence signals. The time scale of the red fluorescence trace is 200 ns/div., and for the other three traces is 10 ns/div.

splitter, consisting of a dichroic mirror having high reflectivity for wavelengths  $>610$  nm, and high transmissivity ( $>85\%$ ) below 550 nm. For purposes of viewing and measuring the red fluorescence, the dichroic mirror is set at  $45^\circ$ .

The PMT having the S1 photocathode (K2276) views the center of the cell via the beam splitter through either an 894 nm or 852 nm interference filter, as well as a neutral filter of sufficient density to ensure a linear response to the red fluorescence signal. In the measurements to be reported the fluorescence signals from both  $\text{Cs}^*(6P)$  were recorded irrespective of which one was pumped. An example of such a record is shown at the lower left of Figure 5. Note that two signal traces are shown, having a common baseline at the top of the graticule. One signal is the fluorescence from the pumped  $\text{Cs}^*(6P)$  state and is initially offscale in the downward direction. The other signal rises from zero, passes through a peak at approximately 200 ns, and thereafter decays exponentially. After approximately 300 ns, the two signals have almost the same intensity in this particular record and are difficult to distinguish at late times.

The PMT having an S-20 response (Thorn EMI 9816 QB) views the center of the cell through an interference filter centered at 378 nm, in combination with a blue glass filter, Corning CS 7-51 (5 mm). An example of the detected UV pulse is shown at the lower right of Figure 5.

When making quantitative measurements of the UV fluorescence signal, the beam splitter is set normal to the viewing axis and a mask is mounted on the beam splitter surface. This mask has a rectangular aperture which acts as field stop, having dimensions such that the image of a 1.0 cm length of the cell axis is transmitted. The green beam is known to have a diameter of  $<1$  mm, and the UV fluorescence will have this same radial extent. In this direction the field stop is given more than sufficient width to transmit the full extent of the image. In this way the exact location of the the image at the field stop is not critical. An adjustable iris is placed close to the outer oven window and used as an aperture stop. Within a calculated range of settings, this fixes the acceptance solid angle from all points on the axial 1 cm selected by the field stop.

Considerable care was necessary to establish conditions where the S-20 PMT used to detect the UV fluorescence signal operates as a linear detector. The pulse amplitude could exceed 1 V with a 50 ohm load, corresponding to 20 mA being drawn from the PMT resistor chain. This is sufficient to lower the voltage across the final dynode stages, thereby lowering the gain. We determined that the tube response remained essentially linear, provided the output pulse amplitude did not exceed 80 mV, and that this constraint could be imposed either by restricting the intensity of the light with neutral density filters or by reducing the tube gain by lowering the applied voltage.

Having established the proper operating conditions for the S-20 PMT, the UV fluorescence signal was recorded either by reading pulse amplitudes from the oscilloscope or by measuring the average PMT output current with an electrometer. The latter measurement was particularly useful for the determination of the total UV fluorescence signal generated per pulse, used to calculate the density of  $Tl_2$  present in the region probed by the green beam.

### 3.2 MEASUREMENTS OF $Cs^*(6P)$ TIME CONSTANTS, AND $Tl_2$ LIFETIMES

As discussed previously (Liu et al., 1986), the time dependence of the red fluorescence is expected to be described by two time constants associated with the rate at which excitation is exchanged between the two levels, and the rates at which the two levels decay. These time constants are predicted by the theoretical model of the filter, and the decay rates of the two levels are of engineering significance in that they affect directly the pump power required in an operational filter. In the present work these time constants were determined under two different operating temperatures of the cell, 400 and 430°C. The procedure used was to photograph the oscilloscope traces of the red fluorescence signals, enlarge the photographs to a convenient size for digitizing the curves, and fit the digitized data to curves of the appropriate double exponential form. For this purpose we used primarily the fluorescence curve of the transferred excitation, since this is well recorded in the early time period where excitation exchange dominates the behavior. An example is shown in Figure 6 of a digitized

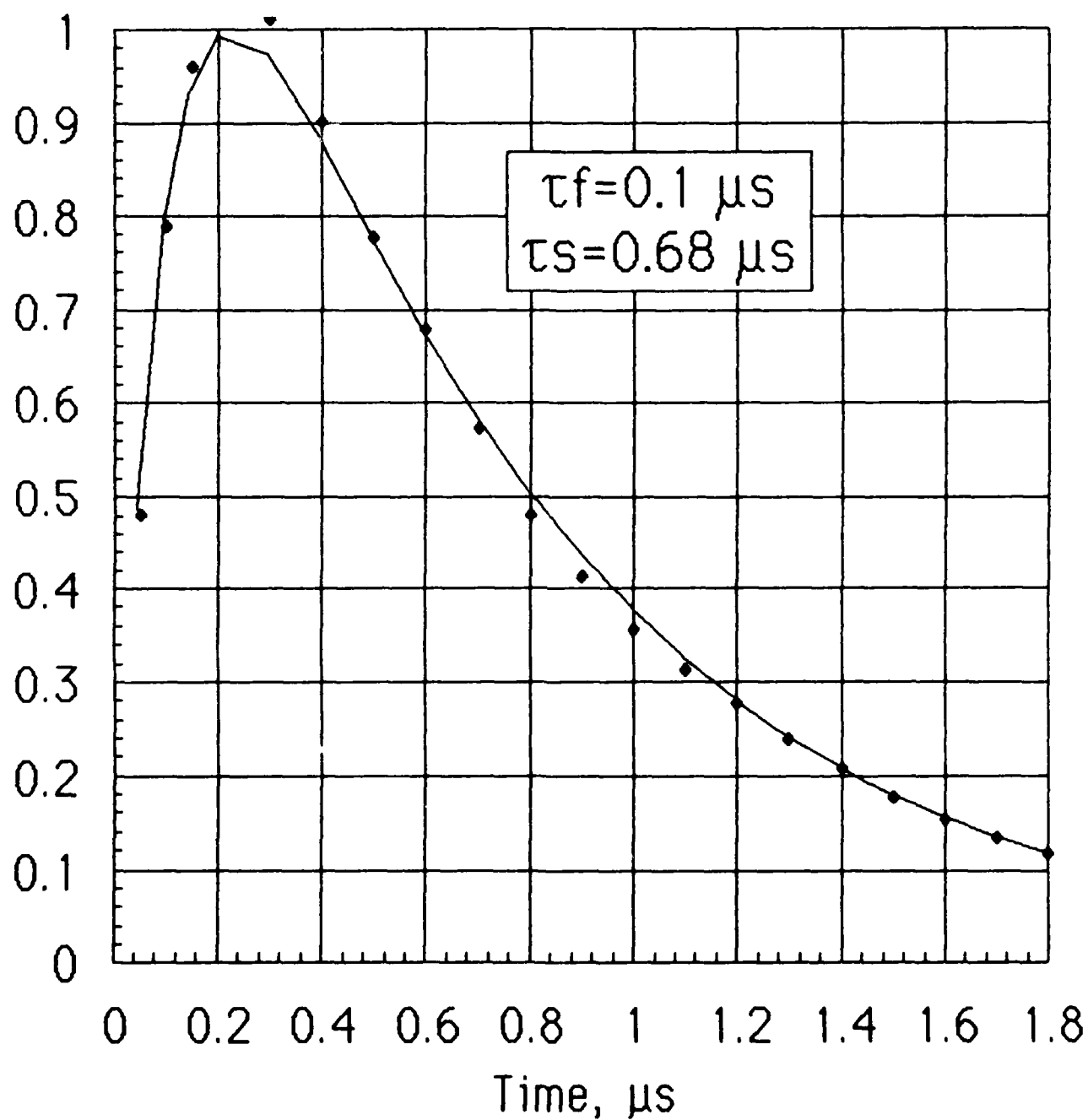


Figure 6. Curve fitting to Cs fluorescence data.



curve and the computer fit from which the two time constants are determined.

Under these same conditions we also recorded the relative signal strengths of the two fluorescence signals, at 852 and 894 nm, using the photographed oscilloscope traces. In reducing the data the measured relative intensities were corrected for the relative transmissions of the two interference filters, and for the decrease in the PMT response between 852 and 894 nm. The two signals have different temporal dependences until late times, and thus we must choose a specific time at which to compare their relative amplitudes. In most instances we chose to do this at the peak of the transferred signal, since this could be easily identified.

Measurements of the time dependence of the density of  $Tl_m$  were made by noting the amplitude of the UV fluorescence pulse produced by fixed intensity green pulse at various delay times after the red pump pulse. The results from these measurements are shown in Figure 7 for the two operating temperatures studied. In each case measurements were made with the red pump beam having its normal radial profile, and also with it expanded by a factor of 2.5. The increased signal achieved with the expanded pump beam is consistent with the intensity being sufficient to burn through the cell. The feature of main interest, however, is the decay time constant of the signal, which reflects the decay time constant of the  $Tl_m$  density. We note that with increased temperature, corresponding to increased Cs and Tl densities, the achieved peak density of  $Tl_m$  increases somewhat, while the  $Tl_m$  lifetime decreases from 1.7 ms to 1.3 ms.

### 3.3 COMPARISON OF MEASURED LIFETIMES, ETC. AND THEORY

The density of the Kr buffer gas within the cell is known from the initial fill, and the density of Tl is assumed to be that given by the vapor pressure data for pure thallium at the measured cold spot temperature. The density of Cs is not known *a priori*, because our knowledge of the Cs vapor pressure over the alloy is only approximate. Therefore, in comparing the measurements described above with theory we regard the Cs density as an unknown. It has been shown previously (Liu et al., 1986) that if level 1 in Figure 2 is pulse pumped, the subsequent time dependences of levels 1 and 2 are given by:

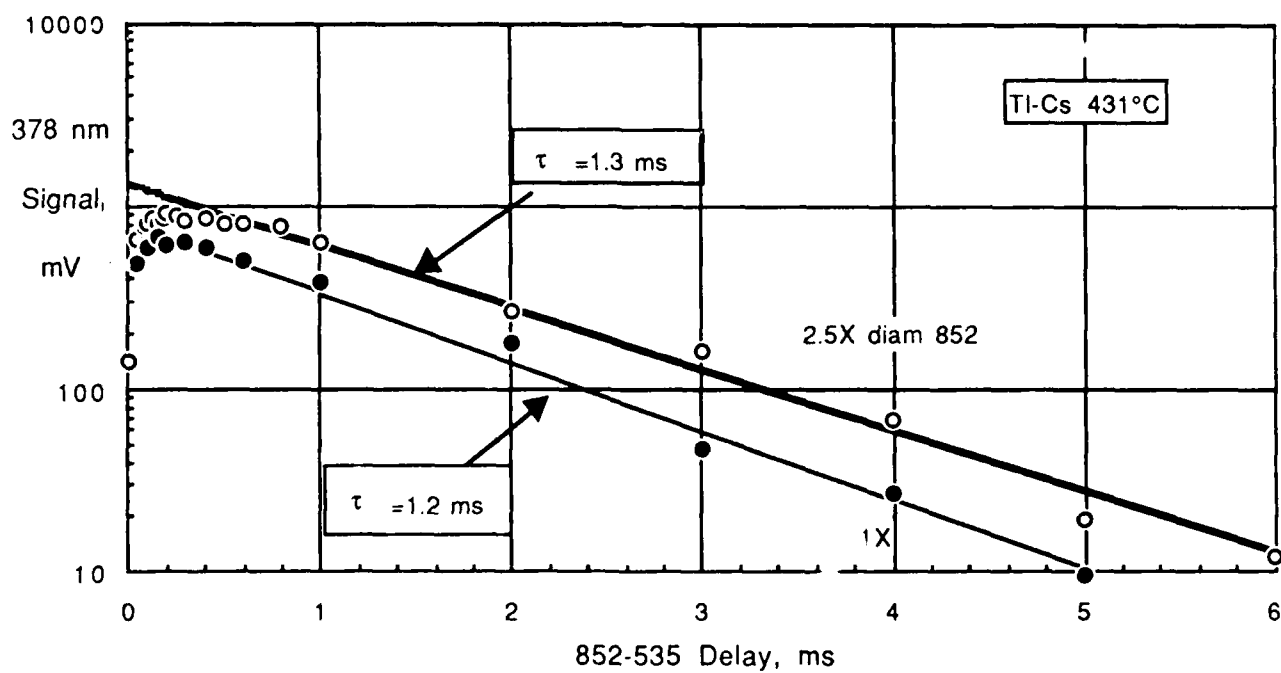
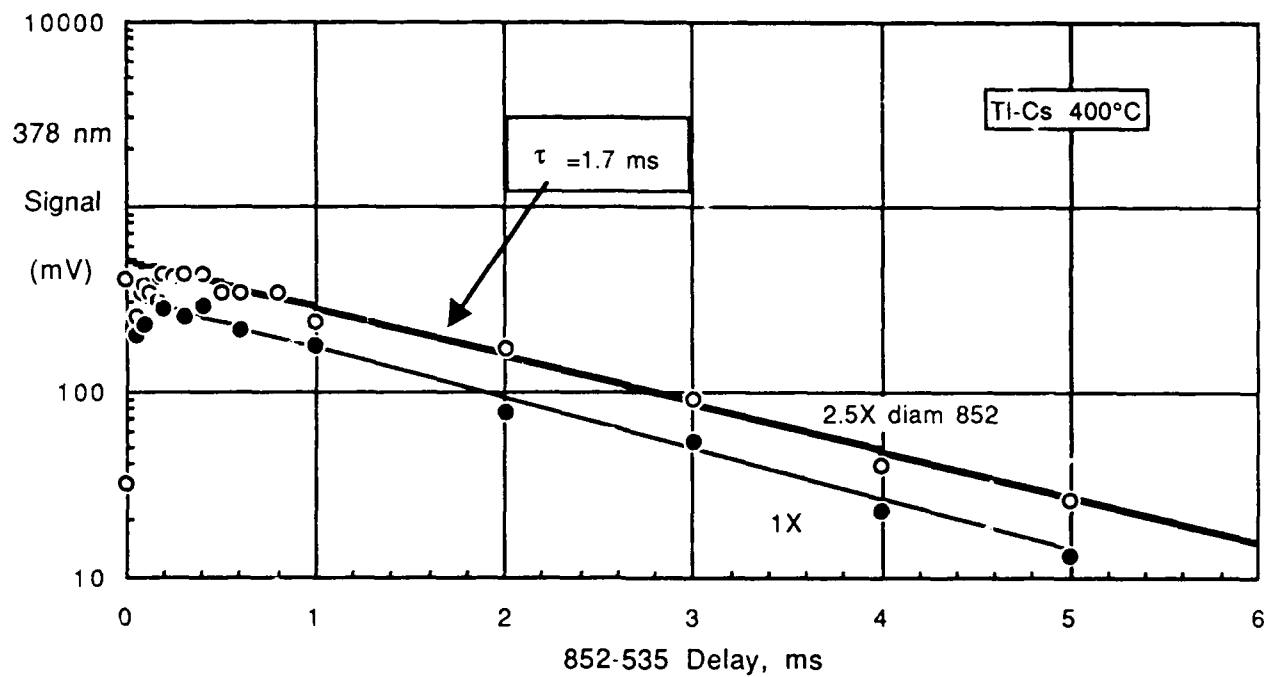


Figure 7. UV fluorescence intensity vs. delay time, measured for two different temperature conditions of the cell. The temperature indicated on each graph is that of the cold spot.

$$N_1(t)/N_1(0) = A_f \exp(-t/\tau_f) + A_s \exp(-t/\tau_s) \quad (1)$$

and 
$$N_2(t) N_1(0) = A [\exp(-t/\tau_s) - \exp(-t/\tau_f)] \quad (2)$$

where 
$$A = K_{12} / [\tau_f^{-1} - \tau_s^{-1}] \quad (3)$$

$$A_f = [K'_1 + K_{12} - \tau_s^{-1}] / [\tau_f^{-1} - \tau_s^{-1}] \quad (4)$$

$$A_s = [\tau_f^{-1} - K'_1 - K_{12}] / [\tau_f^{-1} - \tau_s^{-1}] \quad (5)$$

$$\tau_f^{-1} = \frac{1}{2} \left\{ [K'_1 + K_{12} + K_{21} + K'_2] + \left[ [K'_1 + K_{12} - K_{21} - K'_2]^2 + 4K_{12}K_{21} \right]^{1/2} \right\} \quad (6)$$

$$\tau_s^{-1} = \frac{1}{2} \left\{ [K'_1 + K_{12} + K_{21} + K'_2] - \left[ [K'_1 + K_{12} - K_{21} - K'_2]^2 + 4K_{12}K_{21} \right]^{1/2} \right\} \quad (7)$$

where 
$$K'_{1,2} = K_{1,2} + K_{1,2m}$$

We note from Eq. 2 that  $N_2(t)$  peaks at time

$$t_p = \ln [\tau_s / \tau_f] / [\tau_f^{-1} - \tau_s^{-1}] \quad (8)$$

In the above the subscripts, "f" and "s" indicate the fast and slow components of the double exponential behavior.

The fast and slow time constants,  $\tau_f$  and  $\tau_s$ , are obtained from the data by fitting to Eq. 2, and the results are to be compared with the values given by Eqs. 6 and 7.

The ratio of the densities of the two resonance levels is given by:

$$\frac{N_2(t)}{N_1(t)} = K_{12} \left\{ \frac{\exp(-t/\tau_s) - \exp(-t/\tau_f)}{[K'_1 + K_{12} - \tau_s^{-1}] \exp(-t/\tau_f) - [K'_1 + K_{12} - \tau_f^{-1}] \exp(-t/\tau_s)} \right\} \quad (9)$$

from which we calculate the relative signals using:

$$\frac{S_2}{S_1} = \frac{N_2(t)}{N_1(t)} \cdot \frac{\lambda_1}{\lambda_2} \cdot \frac{\tau_{n1}}{\tau_{n2}} \cdot \frac{g_2}{g_1} \quad (10)$$

where  $\tau_{n1,n2}$  are the natural radiative lifetimes of the resonance lines and  $g_{1,2}$  are their radiation escape factors calculated for the prevailing conditions (Liu et al., 1986). This ratio is to be compared with the ratio of the measured fluorescence signals, taking into account their relative detection efficiencies as discussed above in Section 3.2.

As indicated in Figure 2, the decay time constant of  $Tl_m$  is given by  $K_m^{-1}$ , where  $K_m$  is the total frequency for converting  $Tl_m$  to ground state  $Tl$ :

$$K_m = \tau_{mn}^{-1} + \tau_{mD}^{-1} + v_5 \sigma_5 [Cs_o] + v_6 \sigma_6 [Tl] + v_{13} \sigma_{13} [M] + S \sigma_3 \quad (11)$$

where  $\tau_{mn}$  [=230 ms] (Alexandrov et al., 1978) is the natural radiative lifetime of the metastable level, and  $\tau_{mD}$  is their lifetime against diffusion to the walls, where they are assumed to be quenched. This is calculated from (Chantry, 1987):

$$\tau_{mD} = 2\ell_o/v_o + \Lambda_o^2 \sum (N_i/(D_m N)_i) \quad (12)$$

$$\text{where} \quad \ell_o = \text{Volume/Surface Area} = RL/2(R + L) \quad (13)$$

$\Lambda_o$  is the conventional diffusion length, given by:

$$(1/\Lambda_o)^2 = (\pi/L)^2 + (2.405/R)^2 \quad (14)$$

The normalized diffusion coefficients,  $D_{mi}N_i$ , for diffusion of  $Tl_m$  in  $Tl$  and  $Kr$  are taken from the literature (Aleksandrov et al., 1978), and for diffusion through  $Cs$  we use an estimated value of  $6 \times 10^{18} \text{ cm}^{-1} \text{ s}^{-1}$ .

When the present best estimates of the parameters involved are used in the calculations, we obtain the results represented by the full curves in Figure 8. The experimental measurements of the predicted

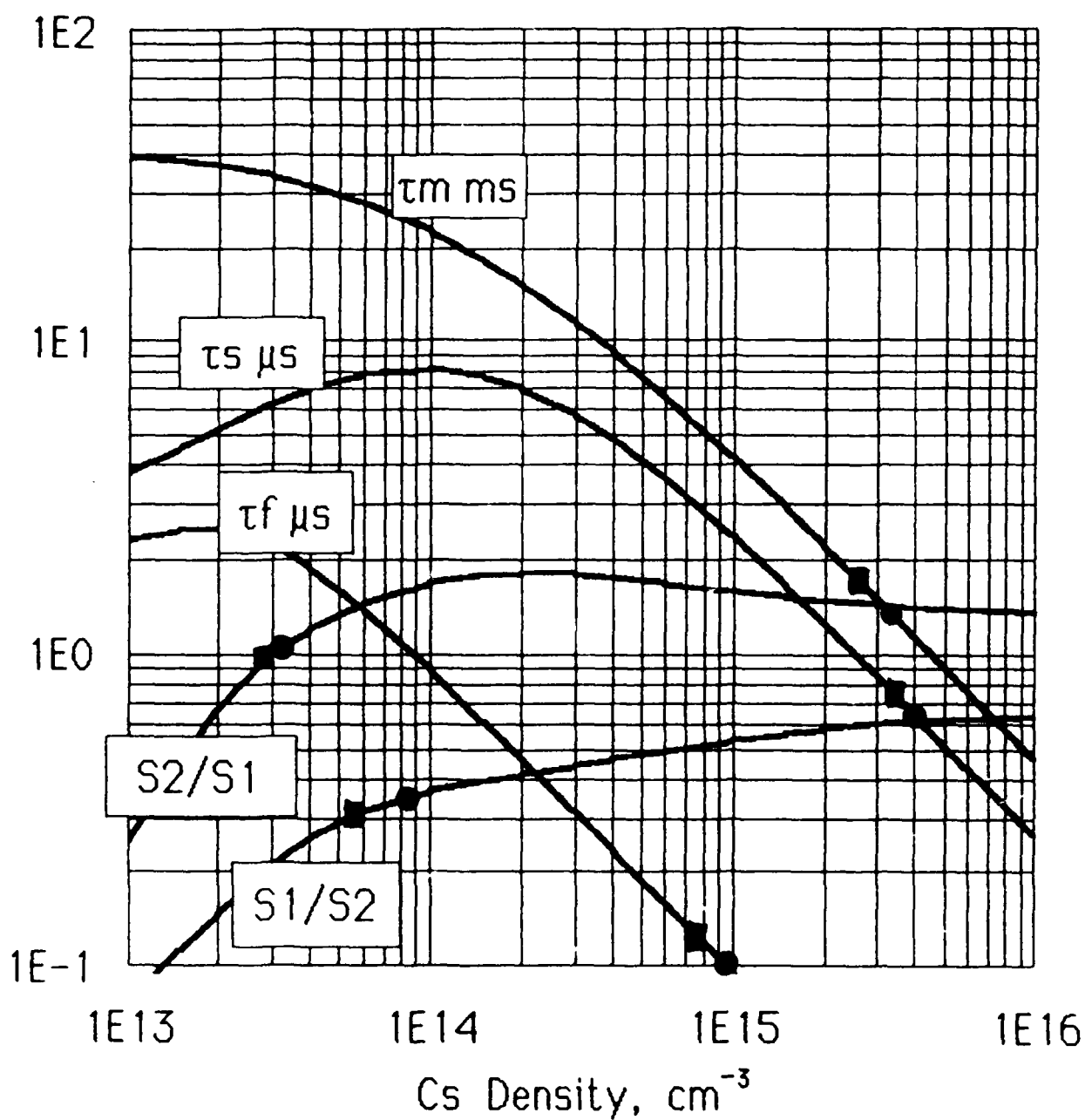


Figure 8. Comparison of measured and predicted fluorescence lifetimes using baseline model parameters from Table 1. The points are from experiments at cold spot temperatures of 400°C (squares) and 430°C (circles).

quantities,  $\tau_f$ ,  $\tau_s$ ,  $\tau_m$ ,  $S_1/S_2$ , and  $S_2/S_1$ , are plotted as points in this figure. The square points are the values measured at a cold spot temperature of 400°C, and the circles are for 430°C. Each data point is plotted on the corresponding theoretical curve and should in principle provide a measure of the Cs density for that measurement. It follows that all the points for the same cold spot temperature should line up at a single value of the abscissa. This clearly does not occur, from which we conclude that our theoretical predictions must be in error, probably from the use of one or more incorrect input parameters.

The most obvious discrepancy between the measured and predicted quantities is that the measured time constants for decay of the metastables,  $\tau_m$ , and the slow time constant for the Cs fluorescence decay,  $\tau_s$ , are both much shorter than predicted by the model. This suggests that additional quenching processes are operating, possibly due to the presence of unknown impurities. To test this hypothesis we have repeated the calculations with additional quenching included. It is convenient to do so by increasing the cross sections for quenching by the buffer gas Kr, but it must not be inferred that the baseline values for these processes are in error. Revised values were chosen by trial and error to give the best consistency within each set of data points at the two temperatures studied. The cross sections for quenching of the Cs\*(6P) states by Kr were increased from their baseline value of  $1 \times 10^{-19} \text{ cm}^2$  to  $1.65 \times 10^{-18} \text{ cm}^2$ , and the cross section for Kr quenching  $Tl_m$  increased from  $1.2 \times 10^{-22}$  to  $8 \times 10^{-20} \text{ cm}^2$ . The results are shown in Figure 9. With this procedure we obtain considerably improved clustering of the points about two specific Cs densities, with the spread being decreased from more than two decades in Figure 8 to approximately a factor of three in Figure 9. We conclude that at these cold spot temperatures, 400 and 430°C,  $[Cs] \sim 3.5 \times 10^{14}$  and  $6 \times 10^{14} \text{ cm}^{-3}$ , respectively. While considerable uncertainties are clearly attached to these numbers, they show the expected trend with temperature and are within the range expected at these temperatures from the alloy recipe used. We shall use these estimates of the Cs density in later analysis of the measured UV fluorescence intensity.

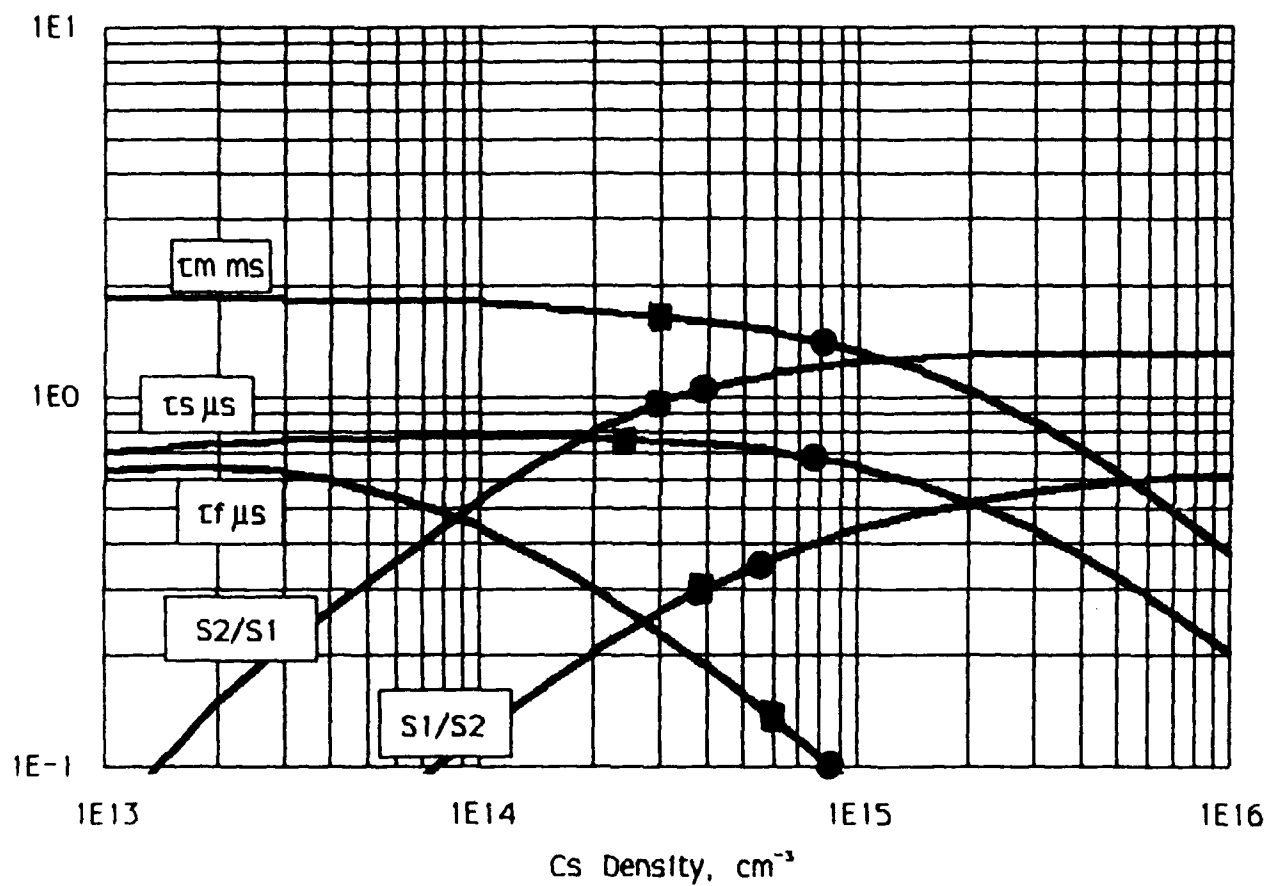


Figure 9. Comparison of measured and fluorescence lifetimes and model predictions using adjusted quenching rates.

### 3.4 DERIVATION OF $[Tl_m]$ FROM THE UV FLUORESCENCE INTENSITY

In order to measure the density of  $Tl_m$  corresponding to the UV fluorescence signals represented in Figure 7, it is necessary to determine the following factors:

- (1) The number of UV photons reaching the S-20 PMT.
- (2) The net transmission efficiency of the optical components (windows, filters, etc.) between the cell axis and the PMT.
- (3) The optical system's acceptance solid angle, normalized to  $4\pi$ .
- (4) The volume of the region probed by the green beam within the 1 cm axial length determined by the field stop. In other words, we need to know the cross-sectional area of the probing beam.
- (5) The probability that a  $Tl_m$  atom within the probed volume results in the emission of a UV photon at 378 nm.

The first factor is determined from the measured average signal current, knowing the photocathode quantum efficiency and the gain of the tube at the operating voltage. The quantum efficiency is read from the manufacturers data at 378 nm, and the gain is determined as a function of voltage by measuring the tube output for a fixed input signal over a range of voltage which includes the test point data supplied with the tube.

The second factor is determined from the individual transmission factors for each of the components. For the bulk glass and interference filters used we relied on the manufacturer's specifications. For lenses and windows, all uncoated, we used a net transmission factor of  $(0.96)^n$  where  $n$  is the number of surfaces involved.

The third factor, the acceptance solid angle normalized to  $4\pi$ , is  $7 \times 10^{-3}$ , calculated from the design of the optical system discussed in Section 3.1.3. The fourth factor, corresponding to a 1 cm length of a cylinder 0.8 mm in diameter, is  $5 \times 10^{-3} \text{ cm}^3$ , determined from the diameter



of the probing green beam measured using an adjustable iris and small circular apertures.

The fifth factor, hereafter called the "yield," is the most difficult to determine. In general it depends on the spectral intensity of the green beam over the absorbing linewidth at 535 nm, the pulse duration, and the strength of the transition. The latter is known from the literature, but to determine the former we must know the green laser linewidth and total intensity, and the absorption linewidth.

Fortunately, we have been able to avoid the uncertainties involved in determining these various quantities by operating the green probe beam at sufficiently high power density to be close to saturation of the 535 nm transition. This is achieved in part by compressing the green beam by a factor of ten in diameter, from 8 to 0.8 mm.

The degree of near saturation is determined by measuring the UV fluorescence intensity as a function of the green beam intensity, and fitting the observed nonlinear behavior to theory. The results are shown in Figure 10, where the points are the relative UV fluorescence signal measured at four values of the green probe beam intensity, controlled by known factors using neutral density filters. These points have been fitted to the heavy full curve obtained theoretically. The ordinate is the yield calculated as a function of the normalized pump power, defined as the pumping frequency per metastable, divided by the net decay rate of the upper state by spontaneous emission of either 378 or 535 nm. The derivation of the theoretical curve is given in Appendix A. From the fit indicated in Figure 10, we conclude that the fluorescence measurement made with the unattenuated green beam corresponds to a normalized pump power of 6.0, and that with these conditions the yield is 0.08.

The value of  $\tau_p=0.34$  used to compute the heavy curve in Figure 10 corresponds to the measured green pulse width obtained from oscilloscope traces, as shown to the upper right of Figure 5. To investigate the sensitivity of the analysis to possible errors regarding the measured pulse width, we also show in Figure 10 curves for significantly higher and lower values of  $\tau_p$ . Their shapes are insignificantly different from the curve used. Fitting the data to these curves would change the derived yield and normalized pump power by at most 20%.

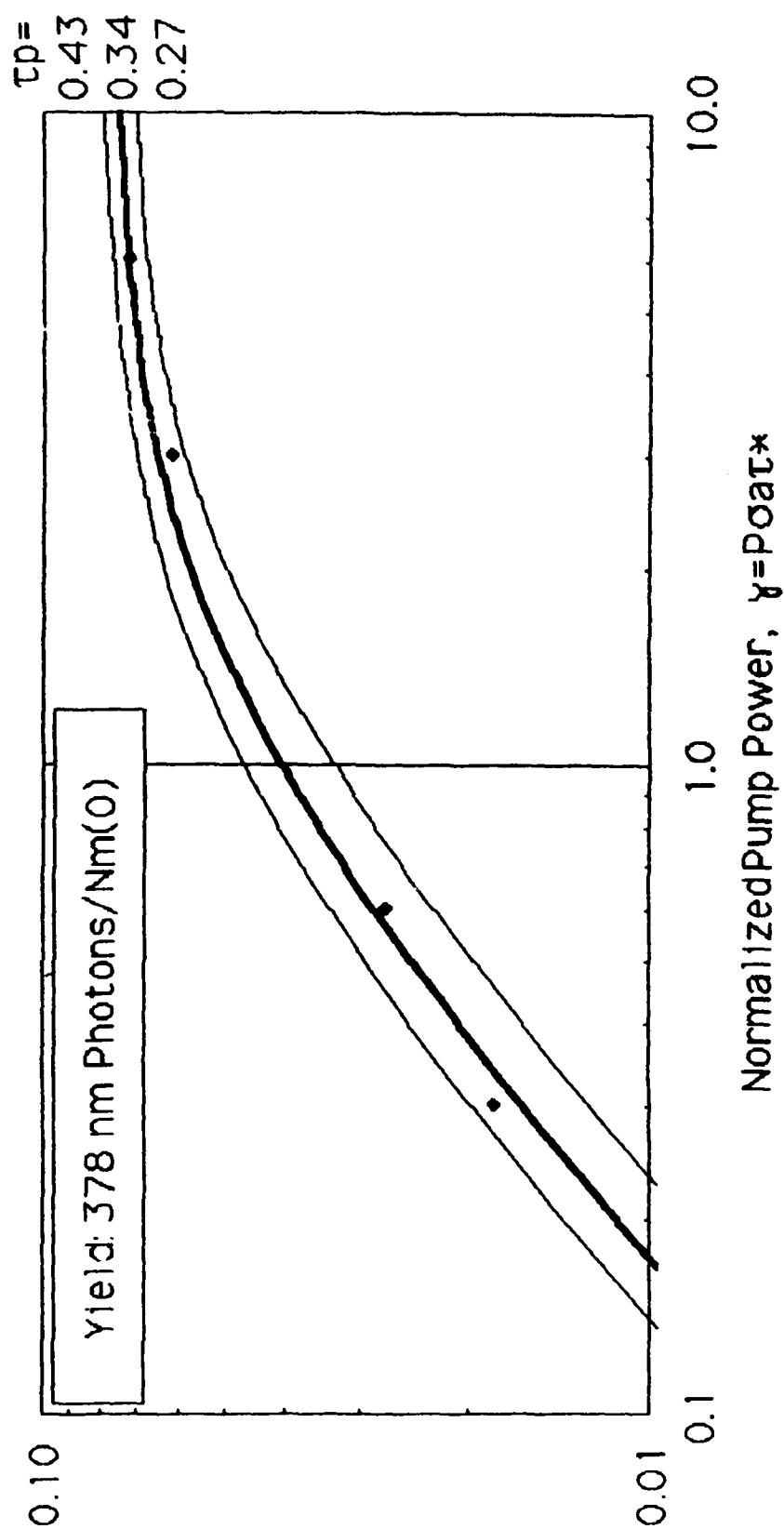


Figure 10. Reconciliation of measured UV intensity vs. 535 nm signal with theoretically predicted curve.

From the analysis presented in Appendix A, we also obtain a predicted UV pulse shape. The curve for the unattenuated beam case, corresponding to the oscilloscope record shown at the bottom right of Figure 5, is shown in Figure 11. As a measure of the pulse width we calculate from the analysis the ratio of area to amplitude, giving in this case a value of  $\bar{w}_p = 15$  ns. This compares well with the value of 16 ns derived from the experimentally measured pulse amplitudes and the corresponding average current, and is consistent with the oscilloscope records, an example of which is shown in Figure 5. We conclude from this comparison of theory and experiment, where the theory involves inclusion of radiation trapping effects, that our model of the processes involved in producing 378 nm photons from  $Tl_m$  is essentially correct.

Using the factors discussed above, we derive a peak thallium metastable density of  $[Tl_m] = 2 \times 10^8 \text{ cm}^{-3}$  achieved on the cell axis using the red pump laser beam without expansion. In order to use this measurement to derive a value for the energy transfer cross section, we need to know the transient density of the  $Cs^*(6P)$  resonance states generated by the red pump laser, and their effective lifetime. The measurement of the latter has been discussed above in Section 3.2

### 3.5 ATTEMPTED MEASUREMENT OF $Cs^*(6P)$ TRANSIENT DENSITY

The peak transient densities of the  $Cs^*(6P)$  resonance states are expected to be sufficiently high in the general vicinity of the axial column pumped by the red beam to permit their detection and quantitative measurement using line absorption along the cell axis. A number of useful transitions exist from both the  $6P_{1/2}$  and the  $6P_{3/2}$  resonance states. For example, a density of  $2.3 \times 10^{11} \text{ cm}^{-3}$  of atoms in the  $6P_{1/2}$  state should give the cell length unit optical density at 566.39 nm, the center of the transition to the  $9D_{3/2}$  state. This wavelength is particularly convenient because it is close to the center of the gain curve for the CW dye laser when operated with Rhodamine 110 dye.

A number of attempts have been made to detect transient absorption at this wavelength, so far without success. The procedure used was to detect the CW laser signal, after transmitting it through the cell, with a fast vacuum photodiode. The beam was preattenuated sufficiently to ensure linear response of the detector, and the diode's

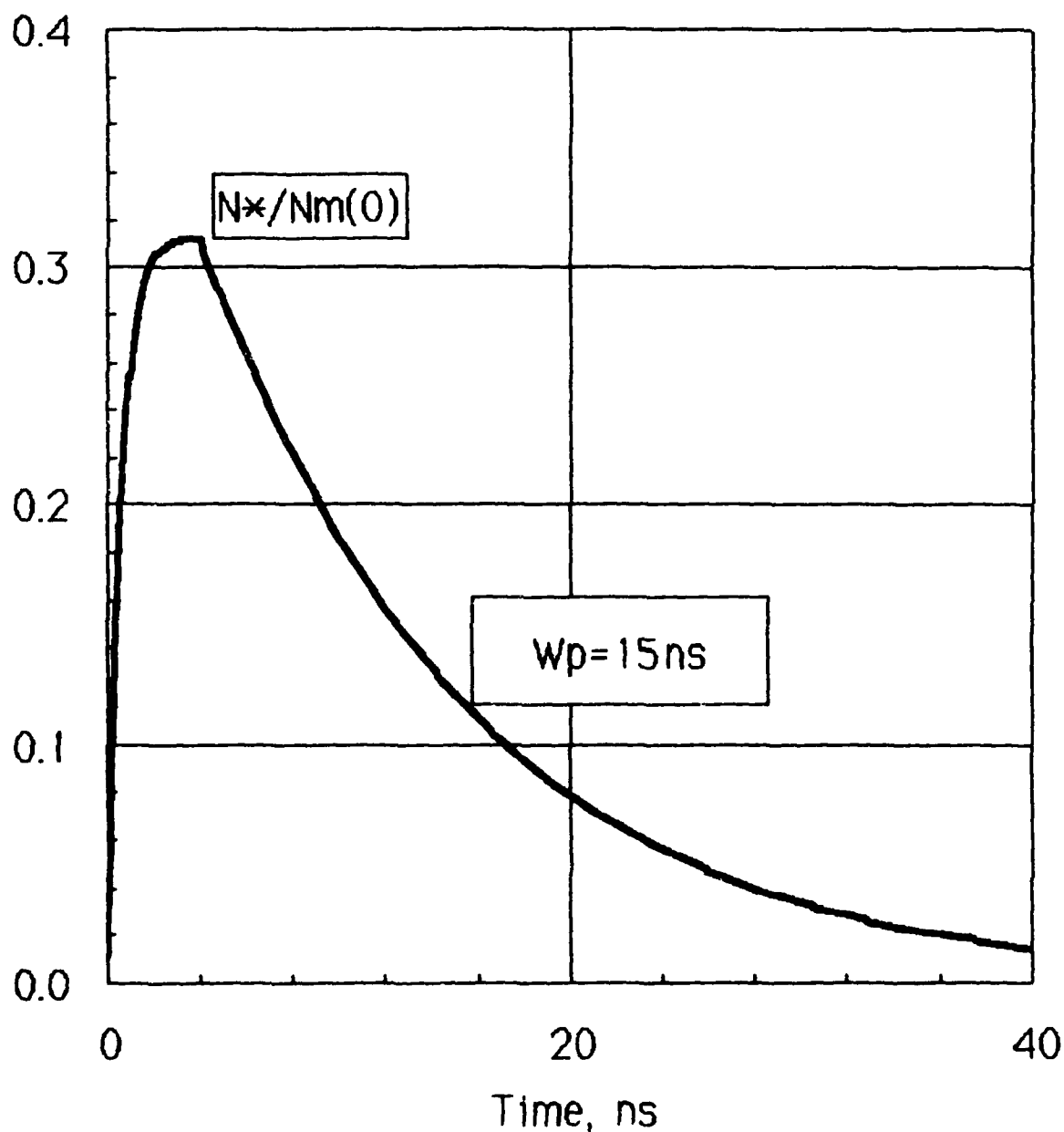


Figure 11. Predicted time dependence of the UV fluorescence signal, taking into account the trapping of the 378 nm line at the density of  $[Tl]=3.6 \times 10^{11} \text{ cm}^{-3}$  expected at the operating cold spot temperature of 430°C. The net radiative lifetime of the upper state under these conditions is 11.6 ns. The indicated pulse width  $W_p$  is the ratio of area to amplitude.

response was displayed on an oscilloscope the time base of which was synchronized to the red laser pump pulse. Using ac coupling of the signal to the oscilloscope preamplifier allowed us to operate such that a dip in the detected signal of a few percent should have been observable. However, tuning the CW laser slowly through the expected position of the absorption line, while watching the repetitive oscilloscope trace, gave no observable dip. One difficulty in performing this experiment is that we did not have available an accurate wavelength reference to assure us that the proper wavelength region was being scanned. The accuracy of the wavemeter used to control the laser wavelength scan should, however, be sufficient for this purpose, and we believe that the explanation of our lack of observable absorption must lie elsewhere.

At the time of writing, our working hypothesis was that our previous attempts to observe absorption may have suffered from laser burnthrough of the medium, due to a combination of the high power density and narrow linewidth of the CW laser. In general, the flux of photons required to bleach a medium is given approximately by:

$$I_{\text{col.sat.}} = \left( \frac{N_a h\nu_{12}}{\tau} \right) \left( \frac{\Delta\nu_{\text{laser}}}{\Delta\nu_{\text{atom}}} \right) \quad (15)$$

where  $N_a$  is the density of absorbers,  $L$  is the cell length,  $\tau$  is the lifetime of the upper state, and the  $\Delta\nu$ 's are the laser and absorption linewidths. The ratio  $\Delta\nu_{\text{atom}}/\Delta\nu_{\text{laser}}$  normally serves to represent the fraction of the laser beam that can be absorbed by the atoms, in the situation where the absorption line is narrow compared to the laser line. In the present case we have the inverse situation; the laser linewidth of 10 KHz is much less than the absorption line width of >900 MHz. In these circumstances it is not clear whether this factor should be retained to represent the fraction of atoms capable of absorbing the laser light. The absorption line center is expected to be dominated by Doppler broadening effects. If the absorbing species velocity vectors are changing frequently due to collisions, compared to the excitation/deexcitation rate, this factor should be replaced by unity. In the present case this may not be the case, and it is possible that

the factor should be retained though possibly in a modified form. Using Eq. (15) suggests that a laser power density of 1 mW/cm<sup>2</sup> would be adequate to cause burnthrough effects with an absorber density of  $\sim 10^{11}$  cm<sup>-3</sup>.

In view of the above discussion, in our future attempts to measure the Cs\*(6P) density by laser absorption we intend to use a photomultiplier as a fast detector, allowing the CW laser beam intensity to be greatly reduced from that used previously, and in addition expanding the beam as much as possible within the constraints of oven windows, etc.

### 3.6 CONCLUSIONS REGARDING THE ENERGY TRANSFER CROSS SECTION, $\sigma_2$

In the absence of a measured value for the peak Cs\*(6P) densities, we are unable to convert our measured value of the peak Tl<sub>m</sub> density into a value for the energy transfer cross section represented by  $\sigma_2$  in Table 1. It is nevertheless instructive to carry the interpretation of the available numbers one step further. We do this by assuming the value of  $\sigma_2 = 2 \times 10^{-17}$  cm<sup>2</sup> estimated from the literature and used consistently in our modelling calculations, and using the data to derive a value for the peak Cs\* density. We can show that with the relative magnitudes of the timeconstants involved, the density of Tl<sub>m</sub> produced is given by:

$$[Tl_m] = [Cs^*] \tau_s v \sigma_2 [Tl_o] \quad (16)$$

where  $[Cs^*]$  is the density of excited Cs produced in the axial region by the red pump pulse,  $\tau_s$  is the timeconstant for the decay of the Cs\* measured by the fluorescence time dependence to be 0.68  $\mu$ s, and  $v$  is the mean thermal velocity of interaction between Cs\* and Tl<sub>o</sub> taken to be  $4 \times 10^4$  cm/s.  $[Tl_o]$  is the ground state density of Tl, calculated to be  $3 \times 10^{11}$  cm<sup>-3</sup> under the conditions of the measurement of  $[Tl_m]$ . The value of  $[Cs^*]$  resulting from Eq. (16) is  $1.2 \times 10^{15}$  cm<sup>-3</sup>. This number is to be compared with the operating density of Cs, which we derived from the analysis presented in Section 3.4 to be  $6 \times 10^{14}$  cm<sup>-3</sup>. Since clearly the Cs\* density cannot exceed the ground state density from which it is formed, we must conclude that one or more of the parameters used in

evaluating  $[Cs^*]$  from Eq. (16) is in error. The only candidate is  $\sigma_2$ , the energy transfer cross section, which must be significantly higher than the value used by at least a factor of three. This would give a derived value of  $[Cs^*]$  equal to that for a fully saturated red transition, with complete coupling of the two  $Cs^*$  states. Hence we derive from the present measurements a lower limit to the energy transfer cross section of:

$$\sigma_2 > 6 \times 10^{-17} \text{ cm}^2 \quad (17)$$

## 4. RADIATION TRAPPING IN ENVELOPES WITH REFLECTING SURFACES

The objective of the work reported in this section was to develop a general algorithm for including the effects of surface reflection in the calculation of the effective radiative lifetime under conditions of radiation trapping. The relevance of this to the Tl-Cs ALF is that the red pump radiation is strongly trapped, and we anticipate that reflecting surfaces would be incorporated in an engineered version in order to further reduce the level of pump power required. In addition, reflecting surfaces are likely to be used in order to direct the UV fluorescence signal to the output window of the cell under circumstances involving a moderate degree of trapping of the UV photons.

So far as we are aware, the only previous work on this topic is that of Weinstein (1962) and of Ingold (1968, 1970). The numerical results of Ingold provide the basis of the present analysis. They refer specifically to the transport of Doppler broadened resonance radiation in a plane parallel enclosure. The earlier paper treats the case of a decaying density of radiating states in an afterglow, while the second is concerned with a steady state discharge situation with the effects of quenching taken into account. Thus the two analyses differ primarily in the spatial distribution of the excited atoms. We shall see, however, that the effect of the reflecting boundaries on the effective lifetime is essentially the same in both situations, at least in the situation where quenching effects are small.

Ingold plots his results as  $\Delta T/RT_0$  vs. the reflection coefficient  $R$ , where  $\Delta T$  is the increase in the trapped lifetime due to the surface reflections, and  $T_0$  is the trapped lifetime for  $R=0$ . The general behavior is similar in shape to the curve of  $(1-R)^{-1}$ , as pointed out by Ingold. This trend is better illustrated in Figure 12 by plotting the same quantity vs.  $(1-R)$  as a log-log plot. The points



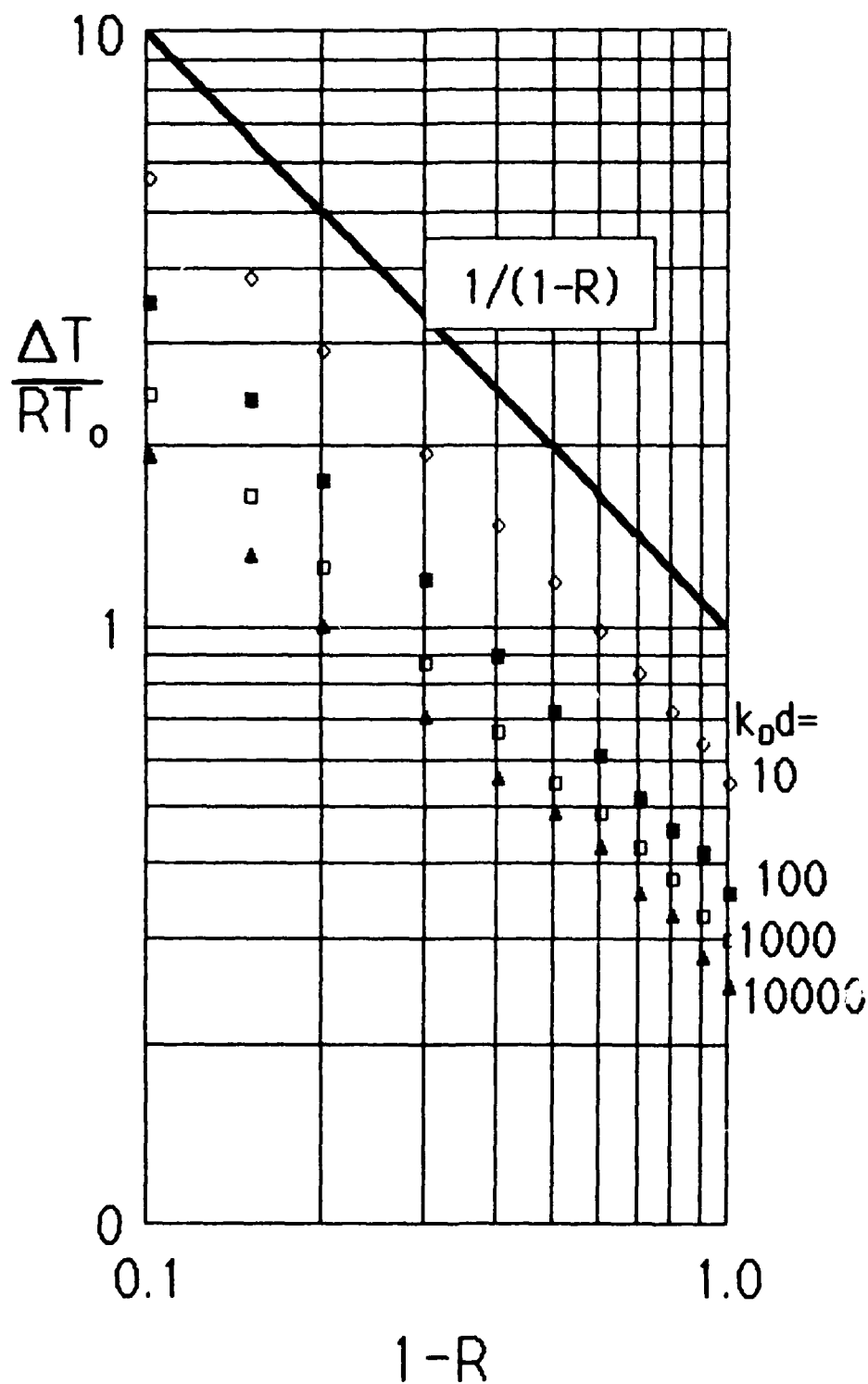


Figure 12. Data from Ingold (1968) replotted to illustrate the  $(1-R)$  dependence.  $T$  is the increase in imprisoned lifetime due to wall reflectivity  $R$ .  $T_0$  is the imprisoned lifetime for  $R=0$ . The parameter  $k_0d$  is the optical depth at line center between the planar boundaries separated by  $d$ .

plotted here are taken from Figure 2 of Ingold (1968). The parametric dependence on the optical depth is shown by the four sets of points for  $k_0 d$  ranging from 10 to 10,000, where  $k_0$  is the absorption coefficient at line center, and  $d$  is the separation of the planar boundaries. We find empirically that this dependence on  $k_0 d$  is suppressed if we plot  $(\Delta T/RT_0)$  weighted by  $[\ln(k_0 d)]^{0.66}$ , in which case the data for all  $k_0 d$  values tends to cluster along the  $(1-R)^{-1}$  line, as illustrated in Figure 13. The data from Ingold's later paper (1970) show the same general trend, as illustrated in Figure 14.

We conclude from the above that for Doppler broadened lines the effect of reflecting boundaries on the trapped lifetime can be approximately calculated from the equation:

$$T(R) = T_0 \left\{ 1 + [R/(1-R)] [\ln(k_0 d)]^{-0.66} \right\} \quad (18)$$

This refers specifically to the case of planar boundaries separated by distance  $d$ , but we can expect the same form to apply to other geometries provided we use the appropriate scale length for that geometry. For example, in the case of a cylinder we expect to replace  $d$  by the radius,  $r$ .

In the absence of appropriate numerical data we cannot test the applicability of Eq. 18 to other line shapes, such as the Lorentzian shape expected for collisionally broadened transitions. However, we expect the same general behavior to occur, and serious error should not result from using this algorithm for lineshapes other than Doppler.

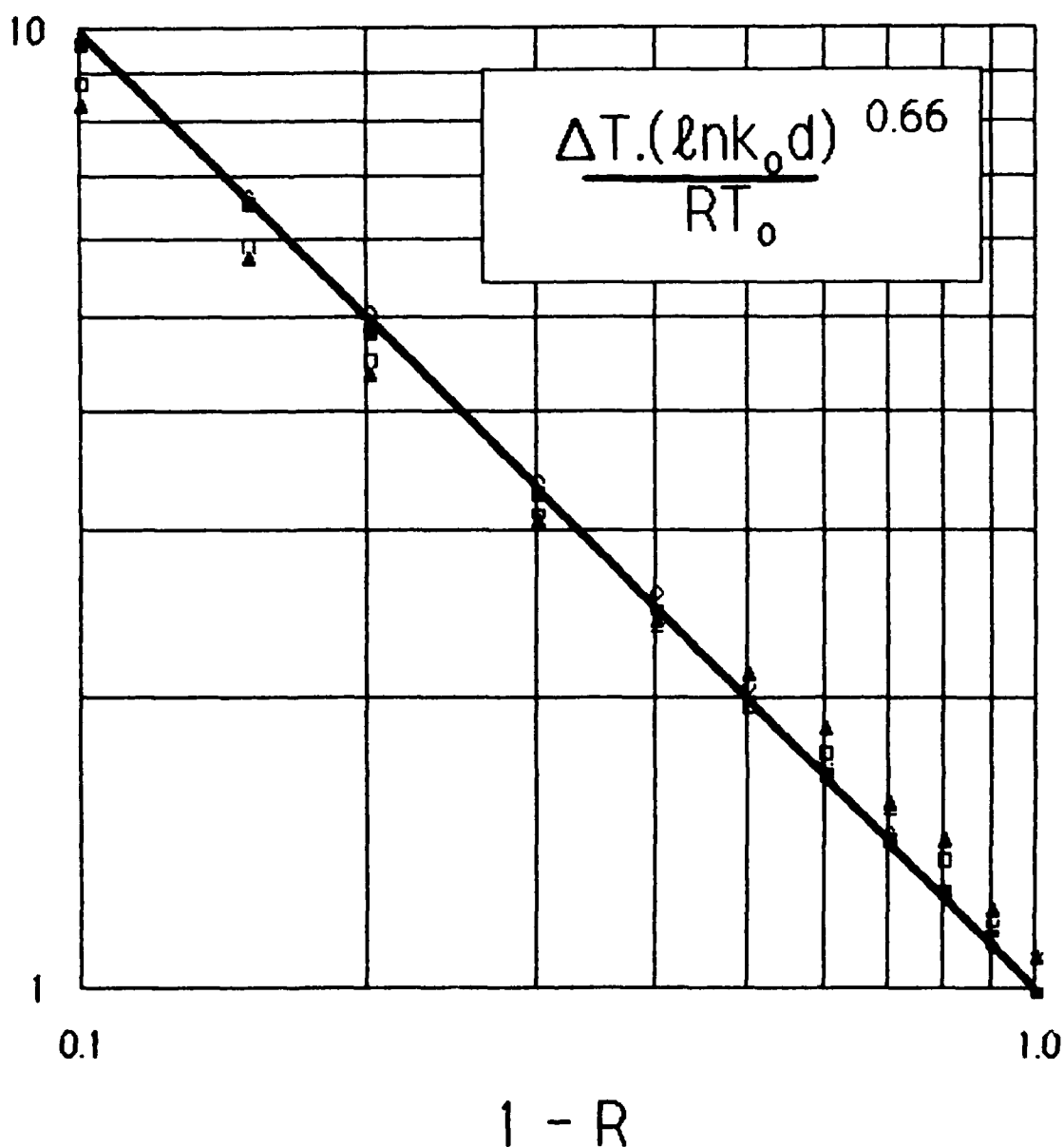


Figure 13. Data from Ingold (1968) replotted to illustrate empirically derived functional form of the dependence on  $k_0 d$ .

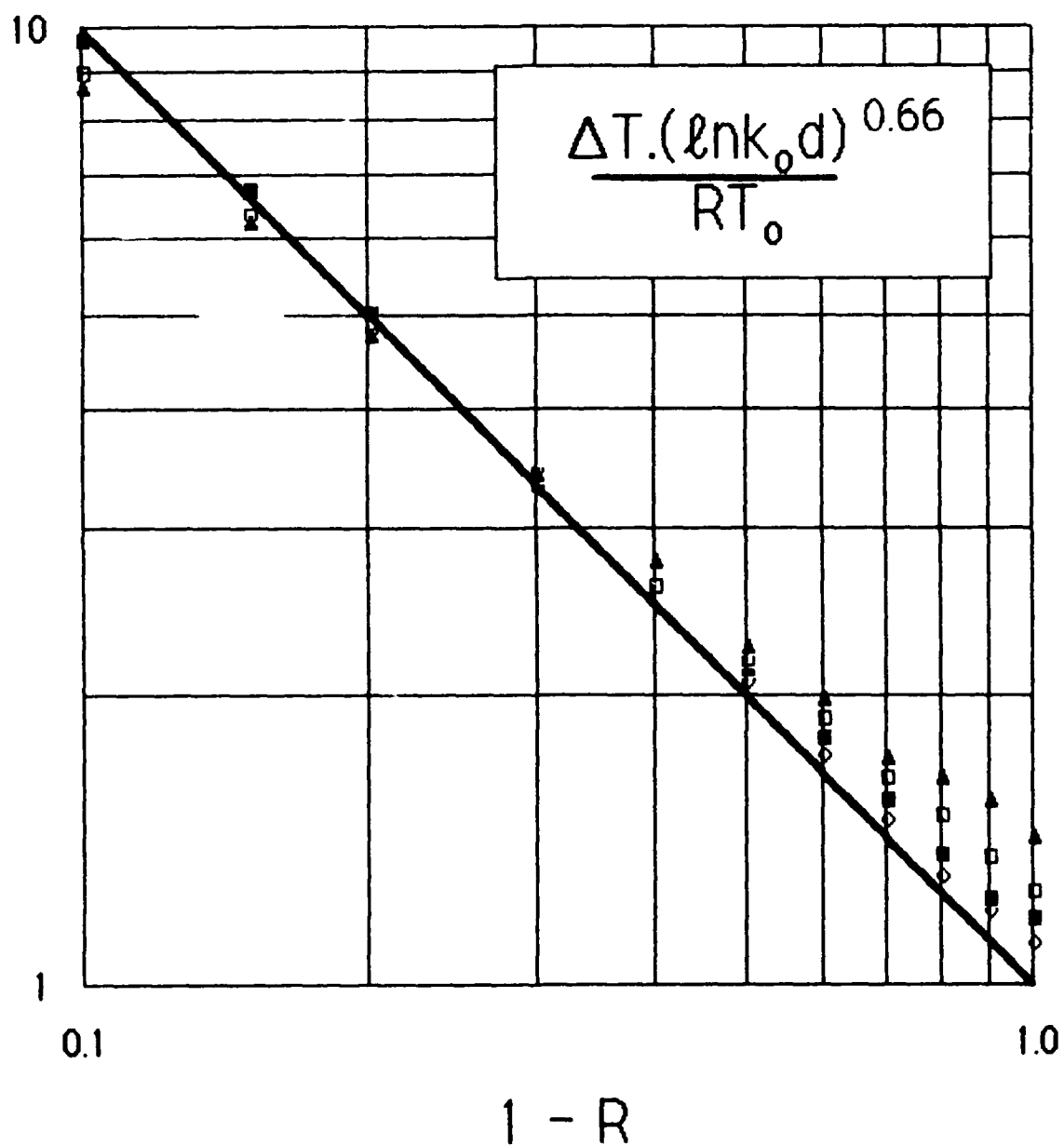


Figure 14. Data from Ingold (1970) replotted using the functional form of the dependence on  $k_0 d$  derived empirically from Ingold's 1968 data, as illustrated in Figure 13.

## 5. CONCLUSIONS AND RECOMMENDATIONS

The results obtained in the present work, while incomplete in the sense that we were unable to measure the density of  $\text{Cs}^*(6P)$  generated in the experiment, are nevertheless useful and encouraging. The derived lower limit for the energy transfer cross section is larger by a factor of three than that we had estimated from the literature. This factor translates to a proportional decrease in the predicted pump power requirement. Additional work is needed to complete the measurement of this cross section. Also, in the course of the present work we established that cell envelopes constructed of Pyrex 7740 glass remain resistant to attack by the metal constituents, Cs and Tl, when held at temperatures in excess of  $400^\circ\text{C}$  for more than 4500 hrs.

Other issues which surfaced during the present study also demand further study. In particular, the measured lifetimes of the active species,  $\text{Cs}^*(6P)$  and  $\text{Tl}_m$ , were both lower by a factor of four or five than we predict from theory. We infer from this that the present cell contains impurities which cause quenching of these states. These need to be eliminated in an engineered version of the cell if the pump power requirements are to be kept to a minimum. At present the source and identity of these impurities is unknown. A systematic study involving the fabrication, processing, and filling of a number of cells is recommended in order to trace this problem and eliminate it.

Finally, we propose that measurements of a cell's performance under CW pumping conditions would be a useful and educational exercise, since this is the mode of operation ultimately required of such cells. To date, all experiments have been performed with pulse pumping, and the performance to be expected with CW pumping has been inferred entirely from our theoretical model. It would be valuable experience to confirm these predictions with a CW pumped experiment, even though the available pump power would probably be substantially lower than needed for an operating receiver cell.

Despite these uncertainties we have made significant progress in our understanding of the Tl-Cs system and remain optimistic that a practical ALF can be developed.

## 6. REFERENCES

- Aleksandrov, E. B., Baranov, A. V., and Kulyasov, V. N. (1978), Opt. Spectrosc. (USSR) 44, 624-627.
- Anderson, R. D., James, R. R., and Rockway, J. W. (1989), NOSC Technical Report 1291, April 1989.
- Borodin, V. M. and Komarov, I. V. (1974), Opt. Spectrosc. 36, 145-149.
- Chantry, P. J. (1987), J. Appl. Phys. 62, 1141-1148.
- Chantry, P. J., Bhasavanich, D., Zollweg, R. J., and Liberman, I. (1988), "Feasibility Demonstration of a Metastable Thallium Atomic Line Filter," Final Technical Report to NUSC Contract No. N66604-87-C-1547.
- Chen, C. L., Hirayama, C., Liu, C. S., Bhasavanich, D., Chantry, P. J., and Liberman, I. (1988), "Development of A Metastable Tl Atomic Line Filter," Final Report SPAWAR/NUSC Contract No. N00039-85-C-0030.
- Czajkowski, M. and Krause, L. (1965), Can. J. Phys. 43, 1259-1268.
- Czajkowski, M., Skardis, G., and Krause, L. (1973), Can. J. Phys. 51, 334-342.
- Dodd, J. N., Enemark, E., and Gallagher, A. (1969), J. Chem. Phys. 50, 4838.
- Gallagher, A. (1968), Phys. Rev. 172, 88-96.
- Gelbwachs, J. A. (1988), IEEE J. Q. E 24, 1266-1277.
- Ingold, J. H. (1968), J. Appl. Phys. 39, 5834.
- Ingold, J. H. (1970), J. Appl. Phys. 41, 94.
- Klyucharev, A. N. and Ryazanov, N. S. (1972), Opt. Spectr. (Trans.) 33, 230-232.
- Korchevoy, Yu. P. and Hilko, I. N. (1977), Proc. ICPIG. p 9. (E. Berlin).
- Liu, C. S., Chantry, P. J., and Chen, C. L. (1986), "Atomic Line Spectral Filters for Nd Laser Receivers," Final Report ONR Contract No. N00014-85-C-0035.
- Marr, G. V. and Creek, D. M. (1968), Proc. Roy. Soc. (London) Ser.A 304, 233.
- Pickett, R. C. and Anderson, R. (1969), J.Q.R.S.T. 9, 697-704.
- Weinstein, M. A. (1962), J. Appl. Phys. 33, 587.

## 7. ACKNOWLEDGMENTS

We are grateful for the continued support and interest in the thallium atomic line filter work from Dr. M. White of ONR. We thank Mr. W. E. Dooley for the capable preparation of the filter cells and for his technical support in the experiments. Dr. J. H. Ingold kindly provided enlarged versions of his published figures. The report was typed by Ms. N. J. Matheys and prepared by Ms. G. S. Law.

## 8. APPENDIX A

### TIME DEPENDENCE AND YIELD OF UV FLUORESCENCE

The objective of this analysis is to predict the relationship between the thallium metastable density and yield of UV fluorescence observed when the medium is probed by an intense pulse tuned to the 535 nm transition. The levels involved are represented in Fig. A1. We assume for the purpose of this analysis that the only processes affecting the density of metastables are those indicated in the figure. This assumption is well satisfied, since the decay time constant of the metastables is known to exceed 1  $\mu$ s and the time scale of interest here is <40 ns.

The following equations represent the densities of the metastables and of the upper state by  $N_m$  and  $N^*$ , respectively. The rate equations controlling these quantities are:

$$\frac{dN_m}{dt} = -P\sigma_a N_m + (A_1 + P\sigma_s)N^* \quad (A1)$$

$$\frac{dN^*}{dt} = P\sigma_a N_m - (A_1 + A_2 + P\sigma_s)N^* \quad (A2)$$

It is convenient to use the following dimensionless variables and parameters

$$\tau = (A_1 + A_2)t = t/\tau^* \quad (A3)$$

$$\alpha = A_1/(A_1 + A_2) \quad (A4)$$

$$\beta = \sigma_s/\sigma_a = g_m/g^* \quad (A5)$$

$$\gamma = P\sigma_a \tau^* \quad (A6)$$



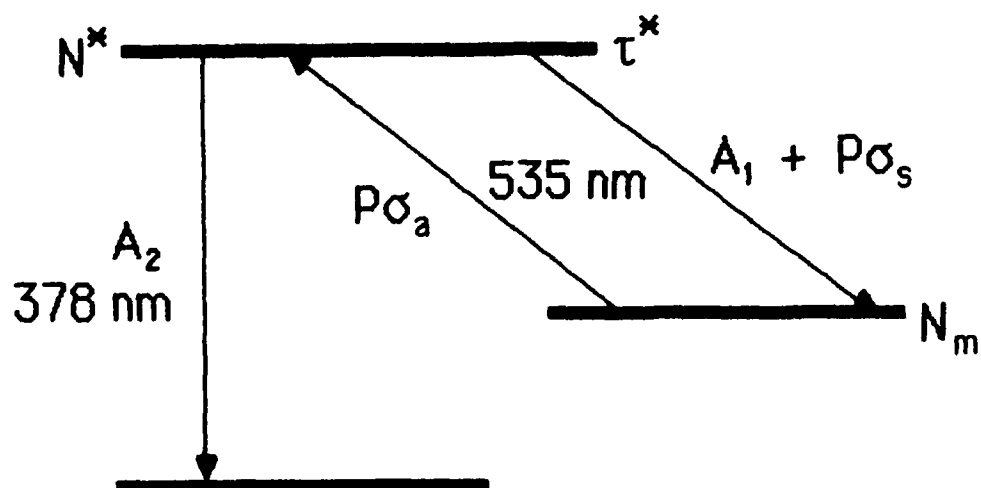


Figure A1. Three-level system involved in the absorption of 535 nm photons by  $Tl_m$ , and the subsequent emission of 535 nm and 378 nm photons by the upper state. The  $A$ 's represent transition probabilities, and  $\sigma$ 's are the stimulated absorption and emission cross sections.  $P$  is the optical power within the absorption linewidth in units of photons/cm<sup>2</sup>/s.

where  $\tau^*$  is the effective spontaneous radiative lifetime of the upper state, and the  $g$ 's in Eq. A5 are the state degeneracies. By further differentiation of Eq. A1 and A2 and substitution, we obtain two independent second order differential equations to be solved by routine techniques. Hence, with the assumption that  $N^*(0)=0$ , we obtain solutions for the period during which the pump pulse is on,

$$N_m/N_m(0) = C_3 \exp(\lambda_1 \tau) + C_4 \exp(\lambda_2 \tau) \quad (A7)$$

$$N^*/N_m(0) = C_5 \{ \exp(\lambda_2 \tau) - \exp(\lambda_1 \tau) \} \quad (A8)$$

where

$$\lambda_1 = 0.5 \left[ C_1 + \sqrt{C_1^2 - 4C_2} \right]$$

$$\lambda_2 = 0.5 \left[ C_1 - \sqrt{C_1^2 - 4C_2} \right]$$

$$C_1 = 1 + \gamma(1 + \beta)$$

$$C_2 = \gamma(1 - a)$$

$$C_3 = (\lambda_2 + \gamma) / (\lambda_2 - \lambda_1)$$

$$C_4 = (\lambda_1 + \gamma) / (\lambda_1 - \lambda_2)$$

$$C_5 = (\lambda_2 + \gamma)(\lambda_1 + \gamma) / (\lambda_1 - \lambda_2)(a + \gamma\beta)$$

For  $\tau \geq \tau_p$ , where  $\tau_p$  is the end of the pump pulse, we solve the same equations with  $\gamma$  set to zero, giving:

$$N^* = N^*(\tau_p) \exp(\tau_p - \tau) \quad (A9)$$

$$N_m = N_m(\tau_p) + aN^*(\tau_p) \{ 1 - \exp(\tau_p - \tau) \} \quad (A10)$$

where the densities at  $\tau_p$  are given by Eq. A7 and A8.

An example of the time dependences of  $N^*$  and  $N_m$  predicted by Eq. A7-A10 is shown in Fig. A2. The value of  $\gamma=6$  used here corresponds to the unattenuated compressed green beam used for the quantitative measurements of the UV fluorescence discussed in Section 3.4. The value of  $\tau_p = 0.34$  corresponds to the measured pulse width of 4 ns. We note that, by the end of the pulse, the ratio of the densities is very close to the factor of two, which would prevail for a fully saturated transition. Following the pulse,  $N^*$  decays with a timeconstant  $\tau^*$ . Due to the trapping of the UV signal under these particular circumstances, there is only 0.18 net branching to the UV transition, compared to 0.47 for no trapping. An optimized cell is expected to operate with moderate trapping, giving 0.3 net branching.

The yield, defined as the fraction of  $N_m(0)$  converted to UV photons by the 535 nm pulse, is given by:

$$Y = 1 - N_m(\infty)/N_m \quad (A11)$$

giving

$$Y = 1 - [C_3 - \alpha C_5] \exp(\lambda_1 \tau_p) - [C_4 + \alpha C_5] \exp(\lambda_2 \tau_p) \quad (A11)$$

In the limit of very intense green power, making  $\gamma$  very large, this becomes:

$$Y = 1 - [(a + \beta)/(1 + \beta)] \exp \left\{ -[(1 - a)/(1 + \beta)] \tau_p \right\} \quad (A12)$$

which in the limit of a very short pulse becomes

$$Y = (1 - a)/(1 + \beta) \quad (A13)$$

As we would expect in this limit, this is equal to the fraction in the upper state with the 535 nm transition fully saturated, multiplied by the UV branching fraction.

The full curve plotted in Fig. 3.8 is calculated from Eq. A11, treating  $\gamma$  as the variable, and using parameter values  $A_1=7.04 \times 10^7 s^{-1}$ ,  $A_2=1.55 \times 10^7 s^{-1}$ ,  $g_m=4$ ,  $g^*=2$ . The value used for  $A_2$  takes into account the effects of radiation trapping on this transition, and is significantly smaller than the natural  $A$  value of  $6.25 \times 10^7 s^{-1}$  for this transition.

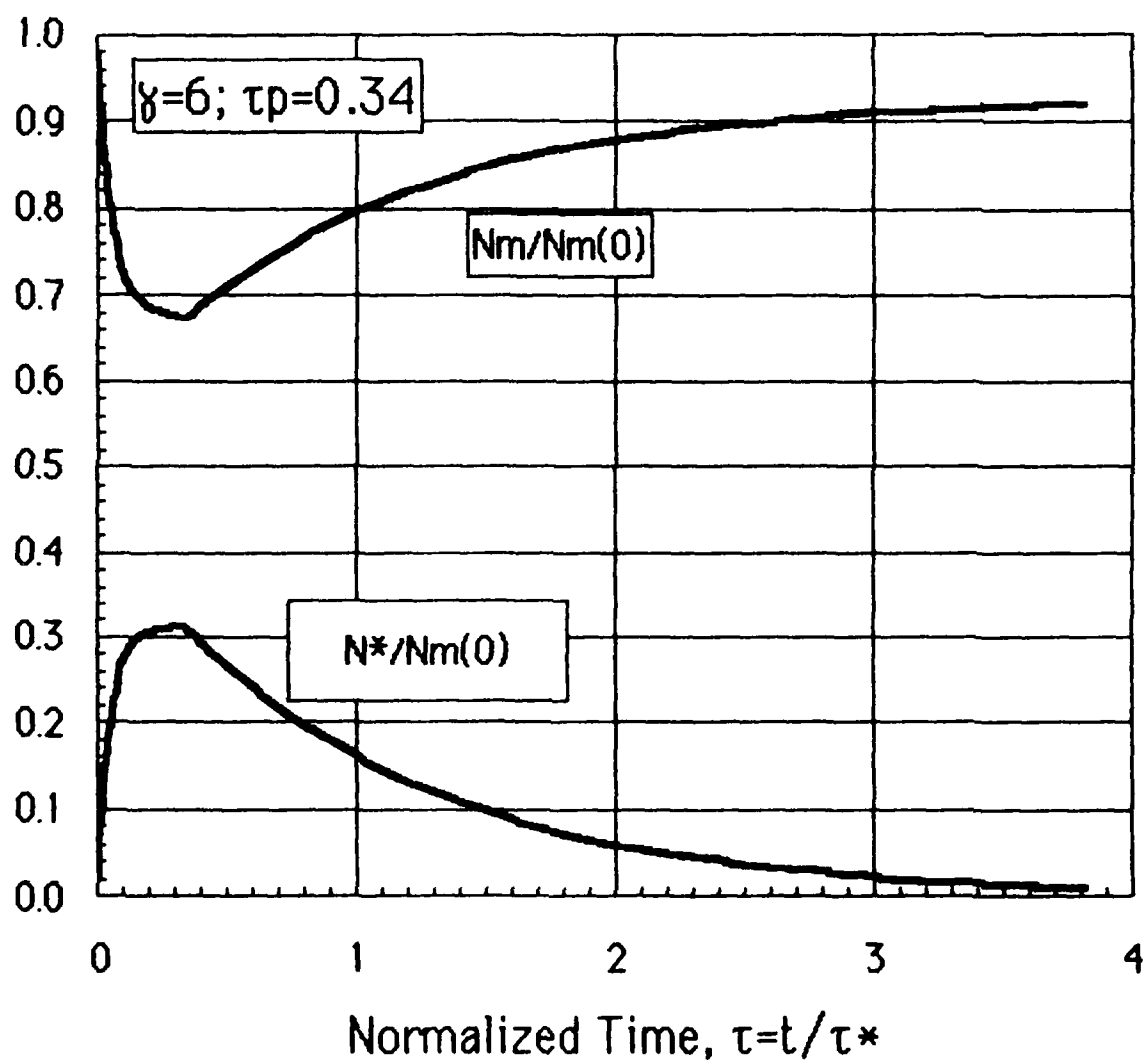


Figure A2. Predicted time dependences of the metastable and excited state densities normalized to the initial metastable density. The ordinate represents time measured in units of the net radiative lifetime of the upper state. The green pump pulse is assumed to last 4 ns.